Scalable processing for realizing 21.7% efficient all-perovskite tandem solar modules

Ke Xiao[1,5], Yen-Hung Lin[2], Mei Zhang[1], Robert D. J. Oliver[2], Xi Wang[3,4], Zhou Liu[1], Xin Luo[1,5], Jia Li[4], Donny Lai[4], Haowen Luo[1], Renxing Lin[1], Jun Xu[5], Yi Hou[3,4], Henry J. Snaith[2]*, and Hairen Tan[1]*

[1]National Laboratory of Solid State Microstructures, Jiangsu Key Laboratory of Artificial Functional Materials, College of Engineering and Applied Sciences, Frontiers Science Center for Critical Earth Material Cycling, Nanjing University, Nanjing 210023, China.

[2]Clarendon Laboratory, Department of Physics, University of Oxford, Oxford OX1 3PU, UK.

[3]Department of Chemical and Biomolecular Engineering, National University of Singapore, 4 Engineering Drive 4, 117585 Singapore

[4]Solar Energy Research Institute of Singapore (SERIS), National University of Singapore, 7 Engineering Drive 1, 117574, Singapore.

[5]School of Electronics Science and Engineering, Nanjing University, Nanjing 210093, China.

*Correspondence to: hairentan@nju.edu.cn (H.T.); henry.snaith@physics.ox.ac.uk (H.J.S)

Challenges in fabricating all-perovskite tandem solar cells as modules rather than as single-junction configurations include growing high-quality wide-bandgap perovskites and mitigating irreversible degradation caused by halide and metal interdiffusion at the interconnecting contacts. We demonstrate efficient all-perovskite tandem solar modules using scalable fabrication techniques. By systematically tuning the cesium ratio of a methylammonium-free 1.8 eV mixed halide perovskite, we improve the homogeneity of crystallization for blade-coated films over large areas. An electrically conductive conformal "diffusion barrier" is introduced between interconnecting subcells to improve the power conversion efficiency (PCE) and stability of all-perovskite tandem solar modules. Our tandem modules achieve a certified PCE of 21.7% with an aperture area of 20 square

centimeters and retain 75% of their initial efficiency after 500-hour continuous operation under simulated 1-sun illumination.

Monolithic all-perovskite tandem solar cells show great promise for large-scale photovoltaic applications with the advantage of low-cost solution processing (*1–3*). However, certified power conversion efficiencies (PCEs), which can reach up to 26.4% (*4*, *5*), have only been achieved in small-area devices with lab-scale spin coating techniques that limit scalability. To enable large-area fabrication of perovskite films, deposition techniques such as spray coating (*6*), inkjet printing (*7*), blade coating (*8*, *9*), slot-die coating (*10*, *11*) and vacuum evaporation (*12*) have been reported. Solution-based fabrication routes all involve solvent engineering to modulate the crystallization dynamics, but the current solvent systems for scalable coating of state-of-the-art ~1.5 eV-bandgap perovskite films are incompatible with those of the ~1.8-eV-bandgap wide bandgap (WBG) perovskites needed for all-perovskite tandems (*10*). The higher bromide concentration in WBG perovskites leads to variations in crystallization kinetics, and precursor solutions are limited by the low solubility of lead and cesium bromide salts (*13*). These constraints hinder the scalable fabrication of high-quality WBG perovskites for all-perovskite tandem solar modules (*14*, *15*).

Another challenge in fabricating perovskite solar modules is linked to the reaction of halides and metal electrodes at the interconnecting subcells. The interdiffusion between the perovskite absorber and metal creates deep defect states at either the interface or bulk of perovskites (*16–19*). Unlike small-area perovskite solar cells (PSCs), perovskite solar modules require a three-step laser or mechanical scribing (namely P1, P2, and P3) to connect the subcells in series (*20–25*). The direct contact between perovskites and metal electrodes at the interconnecting areas between cells leads to subsequent halide-metal interdiffusion and limits the performance and stability of modules

(*26*). If the tandem-cell recombination junction is a highly conductive transparent conducting oxide (TCO) (*27–29*), which is often the case, then metal to recombination-layer contact will also lead to short-circuiting of one or both of the sub junctions. Injecting two-dimensional (2D) barrier materials, such as 2D nanostructured graphitic carbon nitride, between subcells can inhibit such interdiffusion (*26*). However, the poor electronic property of these 2D materials adversely causes an undesirable, large hysteresis in the solar modules. Furthermore, adding a 2D diffusion barrier layer between subcells complicates the overall fabrication process and reduces the geometric fill factor (GFF), because it requires two more independent processes (spin-coating and injecting) and necessitates a much wider space gap between subcells. A one-step process to deposit a thin conformal diffusion barrier would not only improve cost effectiveness but also reduce the cell-to-module efficiency gap.

In this work, we controlled the homogeneity of crystallization in WBG perovskites over large areas by tuning the content of monovalent inorganic cation cesium. This strategy enabled the fabrication of 1-cm^2 all-perovskite tandem solar cells with a steady-state PCE of 24.8% through scalable processing techniques. A conformal diffusion barrier (CDB) consisting of atomic layer deposited SnO_2 (ALD-SnO_2) served as both the vertical electron extractor and the lateral diffusion barrier between interconnecting subcells. The CDB inhibited halide-metal interdiffusion and avoided the reaction between perovskites and metal electrode. Using the ALD-SnO_2 based CDB, we demonstrated all-perovskite tandem solar modules with a certified PCE of 21.7% (aperture area = 20.25 cm^2). Encapsulated tandem solar modules retained 75% of their initial performance after aging for 500 hours at the maximum power point (MPP) operation under simulated one-sun illumination in an ambient condition.

We first attempted to blade coat the WBG perovskite films with a composition of $Cs_{0.2}FA_{0.8}PbI_{1.8}Br_{1.2}$ (FA = formamidinium) which was used for spin-coating process in our previous works (*2*, *3*). The relatively volatile solvent 2-methoxyethanol (2-ME) favors rapid deposition of a uniform perovskite film with low bromide contents (*21*, *30*). However, undesirable crystal precipitation occurred when adding WBG perovskite precursors into 2-ME/dimethyl sulfoxide (DMSO) mixed solvent given the limited solubility of lead/cesium bromide salts in 2-ME (fig. S1). A stable and transparent precursor solution was obtained when the WBG perovskite precursors were added to the coordinating *N*,*N*-dimethylformamide (DMF)/DMSO mixed solvent (fig. S1). We used several solvent quenching methods, such as vacuum flashing, hot casting, and gas-quenching, to remove excess DMF/DMSO solvent after the blade coating step, but none of these methods resulted in dense and uniform perovskite layers (fig. S2). We found that optimizing a range of blading parameter spaces, i.e. blade speed, quenching gas pressure and the gap between the blade and the substrate was not enough to obtain high-quality, uniform $Cs_{0.2}FA_{0.8}PbI_{1.8}Br_{1.2}$ perovskite films (fig. S3). We also attempted to blade-coat films with neat FA cation and a composition of $FAPbI_{1.8}Br_{1.2}$; however, the resulted films exhibited obviously non-perovskite δ phase (fig. S4).

We found that the crystal nucleation rate could be controlled by finely tuning the Cs content (denoted as x in $Cs_xFA_{1-x}PbI_{1.8}Br_{1.2}$ formula) in conjunction with a gas-assisted blade coating technique (Fig. 1A). During the gas quenching step, the nucleation process was initiated under supersaturation conditions, which was evident from the wet perovskite film turning brown with increased Cs content (fig. S5). We observed the enlargement of grain sizes and the flattening of film surface with higher Cs incorporation (up to 35 mol%) into the perovskite. For x = 0.35 ($Cs_{0.35}FA_{0.65}PbI_{1.8}Br_{1.2}$) film, we observed the largest grain sizes with a uniform surface, as

observed from scanning electron microscopy (SEM) and atomic force microscopy (AFM) images (Fig. 1B and fig. S6). It should be noted that the grains or grain boundaries seen in SEM and AFM observations are only features of morphological domains or domain boundaries (*31*). The $Cs_{0.35}FA_{0.65}PbI_{1.8}Br_{1.2}$ perovskite film also exhibited the highest crystallinity as indicated by the x-ray diffraction (XRD) patterns (Fig. 1C and fig. S7A).

The grazing-incidence wide-angle x-ray scattering (GIWAXS) and the corresponding diffraction mottling intensity profiles integrated along q = 1.0 $Å^{-1}$ ring are shown in fig. S8. For blade-coated $Cs_{0.35}FA_{0.65}PbI_{1.8}Br_{1.2}$ perovskite films, the diffraction mottling at the azimuth angle of 45° (135°) and 90° became distinct compared with the ambiguous diffraction mottling at 60° (120°) for spin-coated $Cs_{0.2}FA_{0.8}PbI_{1.8}Br_{1.2}$ perovskite films. This new pattern implied that a distinct stacking orientation developed along with (100) crystallographic planes for the WBG perovskite films deposited through gas-assisted blade coating. Large crystal grains grown perpendicular to the substrate throughout the whole film were observed in blade-coated perovskite films (fig. S8). In contrast, smaller grains with multiple grain boundaries throughout the film were formed for spin-coated films. We observed that the grain orientation and crystallinity of blade-coated films were strongly related with the Cs content, which had only a weak impact on spin-coated films (fig. S9).

We noted a linear increase in the bandgap of $Cs_xFA_{1-x}PbI_{1.8}Br_{1.2}$ perovskites when x was increased up to 0.35. However, non-linearity in optical bandgap was seen when $x > 0.35$ (fig. S10) that may have been caused by phase segregation in the perovskite films (fig. S7B). Perovskites with $x < 0.3$ suffered from light-induced phase segregation under high illumination intensities (i.e. 10 suns), which was evident from the multiple emission peaks observed in the steady-state photoluminescence (PL) spectra (fig. S11). The reduced photo-induced phase segregation in film

with $x = 0.35$ could be due to the reduced lattice strain with a higher Cs ratio (*32*) and/or the change in thermodynamics related to the inter-mixing of ions or ion migration within the crystal lattice (*33*, *34*).

We then evaluated the effect of Cs content on the optoelectronic properties and photovoltaic performance of inverted positive-intrinsic-negative (p-i-n) structured WBG PSCs. The $Cs_{0.35}FA_{0.65}PbI_{1.8}Br_{1.2}$ perovskite films showed the longest carrier lifetime, as determined by PL decay (fig. S12). The performance distribution, external quantum efficiency (EQE) spectral response, and steady-state power output of various $Cs_xFA_{1-x}PbI_{1.8}Br_{1.2}$ based devices are summarized in fig. S13, suggesting an optimal composition of $Cs_{0.35}FA_{0.65}PbI_{1.8}Br_{1.2}$. The champion $Cs_{0.35}FA_{0.65}PbI_{1.8}Br_{1.2}$ device achieved a PCE of 17.2%, with an open-circuit voltage (V_{oc}) of 1.266 V, a short-circuit current density (J_{sc}) of 16.8 mA cm^{-2} and a fill factor (FF) of 80.9% (Fig. 1D and table S1). The blade-coated devices ($x = 0.35$) exhibited comparable performance to the spin-coated ones ($x = 0.20$, fig. S14), and the spin-coated devices with various Cs contents showed similar performance (fig. S15).

To understand how the Cs content ($x = 0.2$ to 0.4) affect the performance of blade-coated cells, we measured the transient photovoltage decay under open-circuit condition (fig. S16). The photovoltage-decay lifetime τ of the $Cs_{0.35}FA_{0.65}PbI_{1.8}Br_{1.2}$ device (86 μs) was higher than that of the $Cs_{0.2}FA_{0.8}PbI_{1.8}Br_{1.2}$ device (31 μs), indicating a reduced recombination when the ratio of Cs was increased from 0.2 to 0.35. To further elucidate V_{oc} improvement of the PSCs with various Cs ratios, we investigated the PL quantum yield (PLQY) of isolated perovskite thin films and device stacks with both charge-transporting layers present (fig. S17). These measured PLQY values were then used to derive the quasi-Fermi level splitting (QFLS) in the respective perovskite materials and p-i-n-stacks (Fig. 1E). Notably, the calculated QFLS values of the p-i-

n-stacks corroborated well with the V_{oc} of the WBG PSCs and suggested that non-radiative recombination losses were reduced by increasing Cs to x = 0.3~0.35.

We then investigated the uniformity of $Cs_{0.35}FA_{0.65}PbI_{1.8}Br_{1.2}$ perovskite films blade coated over a large area (6 cm by 6 cm substrate, fig. S18). We patterned 8 solar cells over a single substrate with each device pixel having an aperture area of 2.2 cm by 1.125 cm (2.475 cm^2), as illustrated in the inset of fig. S19A. All 8 devices showed nearly identical device performance with a minor PCE standard deviation of 0.03% (fig. S19 and table S2). The narrowly distributed device performance indicates the effectiveness of blade coating method to achieve a large-area uniformity for WBG perovskite films. In contrast, the devices distributed on the 6 cm by 6 cm substrate by spin coating exhibited larger variations in performance among 8 pixels (PCE standard deviations = 0.36% and 0.63% for $Cs_{0.35}FA_{0.65}PbI_{1.8}Br_{1.2}$ and $Cs_{0.2}FA_{0.8}PbI_{1.8}Br_{1.2}$, respectively). It should be noted that tuning the Cs content is likely not the only way to achieve high-quality, uniform wide bandgap perovskite films, but further work in optimizing the blading parameter space, precursor solvent and additives, may also lead to similar or even better-quality films.

To realize tandem solar cells with scalable manufacturing techniques, we used blade coating to replace spin coating in all of the solution-based processes, including the fabrication of narrow bandgap (NBG) perovskite film ($MA_{0.3}FA_{0.7}Pb_{0.5}Sn_{0.5}I_3$, where MA is methylammonium) and hole transport layers (Fig. 2A). All other materials layers were deposited through either thermal evaporation or atomic layer deposition (ALD), which are both scalable processes already used in PV manufacturing. The blade-coated NBG PSCs (0.049 cm^2) delivered a champion PCE of 19.0% (steady-state PCE =19.0%) and good reproducibility (fig. S20). Monolithic all-perovskite tandem solar cells, consisting of a ~400 nm thick WBG perovskite and a ~950 nm thick NBG perovskite (Fig. 2B), were fabricated entirely with scalable techniques. The J–V (Fig. 2C) and EQE curves

(Fig. 2D) of the best-performing tandem device with an aperture area of 1.05 cm^2. An average PCE of 23.7 ± 0.7% was obtained among 19 devices (inset of Fig. 2C). The champion device had a PCE of 24.8% from the reverse scan, with a V_{oc} of 2.025 V, a J_{sc} of 15.4 mA cm^{-2} and a FF of 79.4%. A highest efficiency of 25.1% (average PCE of 24.2 ± 0.6% among 44 devices) was obtained for 0.049-cm^2 tandem devices (fig. S21). The relatively modest PCE difference between the 1.05-cm^2 and 0.049-cm^2 cells suggests a good scalability of all-perovskite tandem solar cells.

We fabricated all-perovskite tandem solar modules on 6 cm by 6 cm substrates. The long-term stability and efficiency degradation of perovskite tandem modules is attributed in part to the interfacial halide-metal electrode reaction at the P2 scribed regions between the interconnecting subcells (Fig. 3A). To address this challenge, we devised an electrically conductive conformal diffusion barrier (CDB) by depositing ~10 nm thick SnO_2 using atomic layer deposition technique (ALD-SnO_2) after P2 scribing to avoid interdiffusion and reaction between perovskite and metal electrode (figs. S22 and S23). The CDB layer not only reduces the module manufacturing complexity but also enables a much narrower P2 scribed region (thus higher GFF and module efficiency), compared to injecting a wide insulating 2D barrier material at the interconnecting regions (*26*). We noted that another ALD-SnO_2 protective layer (~10 nm) deposited on C_{60} before the P2 scribing was essential to enable the P2 process performed under ambient conditions (Fig. 3B). We speculate that this compact protective layer prevented NBG perovskite from oxidation during exposure to ambient air (*2*).

In comparison, all of the modules without the ALD-SnO_2 protection layer before P2 process showed inferior performance. After P2 process, the ALD-SnO_2 based CDB layer prevented the direct contact between the metal electrode and the perovskite absorber at the P2 scribed regions. It also prevented direct contact between the metal electrode and the conductive PEDOT:PSS in the

recombination layer, which could otherwise lower the shunt resistance. The current-voltage measurements, performed at the ITO/ALD-SnO_2/Ag junction (where ITO is indium tin oxide), showed good ohmic contact with low vertical resistance (fig. S24), suggesting that this semiconducting CDB layer allowed effective electrical interconnection between subcells. The CDB layer improved in both the efficiency and reproducibility of the all-perovskite tandem solar modules (fig. S25A).

We investigated how the subcell width would affect the performance of tandem modules. Increasing the subcell width allows higher GFF and thus potentially higher module efficiency, but this strategy adversely introduces a higher series resistance and hence reduces the FF. We fabricated modules having 3 to 7 subcells with a fixed total area, corresponding to subcell widths ranging from 15 to 6.4 mm (fig. S25B). The GFF is calculated to decrease linearly from 95.0% to 88.3% as the number of subcells increases (Fig. 3C and fig. S26). The optimal performance was achieved for the 4-subcell tandem modules with a width of 11.25 mm and a GFF of 93.3% (Fig. 3C and table S3). We expect that laser scribing (*35*, *36*), instead of mechanical scribing, for P2 and P3 processed could allow even higher GFF and thus higher module efficiency, given the subcell width of tandems used herein being much larger than those reported in single-junction perovskite solar modules (table S4).

We fabricated 50 all-perovskite tandem solar modules with CDB and with a subcell width of 11.25 mm, showing an average PCE of 20.9% (fig. S25A). The performance of single-junction WBG and NBG modules is summarized in fig. S27 and table S5**.** The champion tandem module exhibited a high PCE of 22.5% under reverse scan, with a V_{oc} of 8.137 V, a J_{sc} of 3.60 mA cm^{-2} and a FF of 76.8% (Fig. 3D). Considering a GFF of 93.3%, the active-area efficiency of tandem module reached 24.1% (fig. S28). The tandem module showed a minor hysteresis between reverse

and forward scans (22.5% vs. 22.1%) and a steady-state PCE of 22.5% at V_{max} of 6.7 V measured over 3 min (fig. S29).

A single tandem module under illumination could steadily power a cooling fan (fig. S29 and movie S1) and six tandem modules connected in parallel could charge for a smartphone (movie S2). One module was sent to an accredited independent PV calibration and measurement laboratory (Japan Electrical Safety and Environment Technology Laboratories, JET) for certification. The module delivered a certified PCE of 21.7% (fig. S30), which has been included in recent Solar Cell Efficiency Tables (version 59) (*5*). The certified PCE 21.7% of the unique tandem module surpasses those of single-junction perovskite solar modules with areas > 10 cm^2 (Fig. 3E and table S4). The PCE of our tandem cell (~ 1 cm^2) using scalable fabrication delivered a comparable performance with those made by spin coating (table S6).

The encapsulated modules with CDB maintained their initial PCE after dark storage for 1778 h under ambient condition with a relative humidity of ~40% (fig. S31). We also tested the operating stability of encapsulated modules in ambient conditions under constant simulated one-sun AM1.5 G illumination. The module with CDB maintained 75% of its initial PCE (22.1%, fig. S32) after 500 h of MPP tracking, whereas the module without CDB degraded below 50% of its initial PCE after 20 h (Fig. 4A). We reasoned that the performance degradation of the module with CDB was not attributed mainly to the WBG perovskite; the single-junction WBG module could maintain 95% of its initial PCE after 450 h of MPP tracking (fig. S33). The faster degradation for the tandem modules with CDB than the single-junction WBG module could be originated from following two reasons: (i) Au as recombination layer could diffuse into the NBG perovskite layer, leading to the formation of defect states at the perovskite interface or in the bulk (*18*), (ii) the reaction at the PEDOT:PSS/NBG perovskite interface led to poorer charge extraction (*37*).

We tracked the thermal stability of encapsulated modules by heating at 85°C in an N_2 glove box. The module without CDB degraded down to 10% of initial PCE after 312 h, while the module with CDB still maintained > 70% of its initial performance (Fig. 4B). For modules without CDB, erosion of the metal electrode was observed after thermal aging at the interconnecting regions (fig. S34). We speculated that the erosion was induced by the halide-metal interdiffusion at the interconnecting regions (lateral edges of the subcells in module) because of the direct contact between perovskite and metal. The halide-metal interdiffusion would have two negative effects, metal diffusion into the perovskite absorber could degrade perovskite and increase charge carrier recombination, and the halide diffusion into the electrode could corrode the metal and reduce its electrical conduction.

To investigate the halide-metal diffusion, we reduced the subcell width in a tandem module to obtain a 1-mm width grid cells at P2 process in order to monitor the I-Ag interdiffusion through x-ray photoelectron spectroscopy (XPS) characterization (fig. S35). The devices were then subjected to heating at 85°C in an N_2 glovebox for 24 hours. For modules without CDB, Ag was detected by XPS in perovskite films when the x-ray beam was placed on the perovskite film surface after peeling off the C_{60}/ALD-SnO_2/Ag multiple layers on top (Fig. 4C and fig. S35). This result indicated that Ag diffused laterally from the P2 region into the perovskite absorbers, whereas the halides (I^-) diffused into the edge metal electrode where it had direct contact with the perovskite (fig. S36). In contrast, for the CBD layer containing modules, no obvious signals of Ag (or I) were detected in perovskite layer (or edge metal electrode), indicating that the I-Ag interdiffusion was effectively suppressed (*18*).

To intuitively elucidate the lateral interdiffusion between perovskite and metal electrode, we further fabricated the following structures: (i) glass/ITO/WBG perovskite (~400 nm)/Ag and (ii)

glass/ITO/WBG perovskite/CDB/Ag, similar to the lateral structure in P2 scribed regions. After thermal aging at 85°C, we performed elemental analysis using scanning electron microscopy with energy-dispersive x-ray (SEM-EDX, fig. S37). The I-Ag interdiffusion occurred across the direct perovskite/electrode contact and extended over the entire perovskite/metal layers, whereas the halide-metal interdiffusion was largely hindered by the employment of CDB. Br-Ag interdiffusion was not observed (figs. S36 and S37), possibly due to the larger electronegativity of Br and thus stronger Pb-Br bonding (*38*).

We speculate that the CDB technique is a universal approach to enhance the efficiency and stability of perovskite solar modules in all types. To facilitate mass production in the future, development of green solvent system (avoiding the use of toxic DMF) should be considered for the manufacturing of all-perovskite tandem solar modules (*39*, *40*).

References

1. G. E. Eperon, T. Leijtens, K. A. Bush, R. Prasanna, T. Green, J. T.-W. Wang, D. P. McMeekin, G. Volonakis, R. L. Milot, R. May, A. Palmstrom, D. J. Slotcavage, R. A. Belisle, J. B. Patel, E. S. Parrott, R. J. Sutton, W. Ma, F. Moghadam, B. Conings, A. Babayigit, H.-G. Boyen, S. Bent, F. Giustino, L. M. Herz, M. B. Johnston, M. D. McGehee, H. J. Snaith, Perovskite-perovskite tandem photovoltaics with optimized band gaps. *Science* **354**, 861–865 (2016).

2. K. Xiao, R. Lin, Q. Han, Y. Hou, Z. Qin, H. T. Nguyen, J. Wen, M. Wei, V. Yeddu, M. I. Saidaminov, Y. Gao, X. Luo, Y. Wang, H. Gao, C. Zhang, J. Xu, J. Zhu, E. H. Sargent, H. Tan, All-perovskite tandem solar cells with 24.2% certified efficiency and area over 1 cm2 using surface-anchoring zwitterionic antioxidant. *Nat. Energy* **5**, 870–880 (2020).

3. R. Lin, K. Xiao, Z. Qin, Q. Han, C. Zhang, M. Wei, M. I. Saidaminov, Y. Gao, J. Xu, M. Xiao, A. Li, J. Zhu, E. H. Sargent, H. Tan, Monolithic all-perovskite tandem solar cells with 24.8% efficiency exploiting comproportionation to suppress Sn(ii) oxidation in precursor ink. *Nat. Energy* **4**, 864–873 (2019).

4. R. Lin, J. Xu, M. Wei, Y. Wang, Z. Qin, Z. Liu, J. Wu, K. Xiao, B. Chen, S. M. Park, G. Chen, H. R. Atapattu, K. R. Graham, J. Xu, J. Zhu, L. Li, C. Zhang, E. H. Sargent, H. Tan, All-perovskite tandem solar cells with improved grain surface passivation. *Nature* **603**, 73–78 (2022).

5. M. A. Green, E. D. Dunlop, J. Hohl-Ebinger, M. Yoshita, N. Kopidakis, X. Hao, Solar cell efficiency tables (version 59). *Prog. Photovoltaics Res. Appl.* **30**, 3–12 (2022).

6. J. E. Bishop, J. A. Smith, D. G. Lidzey, Development of Spray-Coated Perovskite Solar Cells. *ACS Appl. Mater. Interfaces* **12**, 48237–48245 (2020).

7. X. Peng, J. Yuan, S. Shen, M. Gao, A. S. R. Chesman, H. Yin, J. Cheng, Q. Zhang, D. Angmo, Perovskite and Organic Solar Cells Fabricated by Inkjet Printing: Progress and Prospects. *Adv. Funct. Mater.* **27**, 1703704 (2017).

8. Y. Deng, X. Zheng, Y. Bai, Q. Wang, J. Zhao, J. Huang, Surfactant-controlled ink drying enables high-speed deposition of perovskite films for efficient photovoltaic modules. *Nat. Energy* **3**, 560–566 (2018).

9. M. Yang, Z. Li, M. O. Reese, O. G. Reid, D. H. Kim, S. Siol, T. R. Klein, Y. Yan, J. J. Berry, M. F. A. M. van Hest, K. Zhu, Perovskite ink with wide processing window for scalable high-efficiency solar cells. *Nat. Energy* **2**, 17038 (2017).

10. Z. Yang, W. Zhang, S. Wu, H. Zhu, Z. Liu, Z. Liu, Z. Jiang, R. Chen, J. Zhou, Q. Lu, Z. Xiao, L. Shi, H. Chen, L. K. Ono, S. Zhang, Y. Zhang, Y. Qi, L. Han, W. Chen, Slot-die coating large-area formamidinium-cesium perovskite film for efficient and stable parallel solar module. *Sci. Adv.* **7**, eabg3749 (2021).

11. J. B. Whitaker, D. H. Kim, B. W. Larson, F. Zhang, J. J. Berry, M. F. A. M. Van Hest, K. Zhu, Scalable slot-die coating of high performance perovskite solar cells. *Sustain. Energy Fuels* **2**, 2442–2449 (2018).

12. J. Li, H. Wang, X. Y. Chin, H. A. Dewi, K. Vergeer, T. W. Goh, J. W. M. Lim, J. H. Lew, K. P. Loh, C. Soci, T. C. Sum, H. J. Bolink, N. Mathews, S. Mhaisalkar, A. Bruno, Highly Efficient Thermally Co-evaporated Perovskite Solar Cells and Mini-modules. *Joule* **4**, 1035–1053 (2020).

13. N.-G. Park, Crystal growth engineering for high efficiency perovskite solar cells. *CrystEngComm*. **18**, 5977–5985 (2016).

14. Y. Rong, Y. Hu, A. Mei, H. Tan, M. I. Saidaminov, S. Il Seok, M. D. McGehee, E. H. Sargent, H. Han, Challenges for commercializing perovskite solar cells. *Science* **361**, eaat8235 (2018).

15. Y. Hu, Y. Chu, Q. Wang, Z. Zhang, Y. Ming, A. Mei, Y. Rong, H. Han, Standardizing Perovskite Solar Modules beyond Cells. *Joule* **3**, 2076–2085 (2019).

16. E. Bi, H. Chen, F. Xie, Y. Wu, W. Chen, Y. Su, A. Islam, M. Grätzel, X. Yang, L. Han, Diffusion engineering of ions and charge carriers for stable efficient perovskite solar cells. *Nat. Commun.* **8**, 15330 (2017).

17. J. Li, Q. Dong, N. Li, L. Wang, Direct Evidence of Ion Diffusion for the Silver-Electrode-Induced Thermal Degradation of Inverted Perovskite Solar Cells. *Adv. Energy Mater.* **7**,

1602922 (2017).

18. H. Gao, Q. Lu, K. Xiao, Q. Han, R. Lin, Z. Liu, H. Li, L. Li, X. Luo, Y. Gao, Y. Wang, J. Wen, Z. Zou, Y. Zhou, H. Tan, Thermally Stable All-Perovskite Tandem Solar Cells Fully Using Metal Oxide Charge Transport Layers and Tunnel Junction. *Sol. RRL* **5**, 2100814 (2021).

19. C. C. Boyd, R. Cheacharoen, K. A. Bush, R. Prasanna, T. Leijtens, M. D. McGehee, Barrier Design to Prevent Metal-Induced Degradation and Improve Thermal Stability in Perovskite Solar Cells. *ACS Energy Lett.* **3**, 1772–1778 (2018).

20. Y. Deng, S. Xu, S. Chen, X. Xiao, J. Zhao, J. Huang, Defect compensation in formamidinium–caesium perovskites for highly efficient solar mini-modules with improved photostability. *Nat. Energy* **6**, 633–641 (2021).

21. Y. Deng, C. H. Van Brackle, X. Dai, J. Zhao, B. Chen, J. Huang, Tailoring solvent coordination for high-speed, room-temperature blading of perovskite photovoltaic films. *Sci. Adv.* **5**, eaax7537 (2019).

22. S. Chen, X. Dai, S. Xu, H. Jiao, L. Zhao, J. Huang, Stabilizing perovskite-substrate interfaces for high-performance perovskite modules. *Science* **373**, 902–907 (2021).

23. H. Chen, F. Ye, W. Tang, J. He, M. Yin, Y. Wang, F. Xie, E. Bi, X. Yang, M. Grätzel, L. Han, A solvent-and vacuum-free route to large-area perovskite films for efficient solar modules. *Nature* **550**, 92–95 (2017).

24. N. G. Park, K. Zhu, Scalable fabrication and coating methods for perovskite solar cells and solar modules. *Nat. Rev. Mater.* **5**, 333–350 (2020).

25. Z. Liu, L. Qiu, L. K. Ono, S. He, Z. Hu, M. Jiang, G. Tong, Z. Wu, Y. Jiang, D. Y. Son, Y. Dang, S. Kazaoui, Y. Qi, A holistic approach to interface stabilization for efficient perovskite solar modules with over 2,000-hour operational stability. *Nat. Energy* **5**, 596–604 (2020).

26. E. Bi, W. Tang, H. Chen, Y. Wang, J. Barbaud, T. Wu, W. Kong, P. Tu, H. Zhu, X. Zeng, J. He, S. Kan, X. Yang, M. Grätzel, L. Han, Efficient Perovskite Solar Cell Modules with High Stability Enabled by Iodide Diffusion Barriers. *Joule* **3**, 2748–2760 (2019).

27. A. F. Palmstrom, G. E. Eperon, T. Leijtens, R. Prasanna, S. N. Habisreutinger, W. Nemeth, E. A. Gaulding, S. P. Dunfield, M. Reese, S. Nanayakkara, T. Moot, J. Werner, J. Liu, B. To, S. T. Christensen, M. D. McGehee, M. F. A. M. van Hest, J. M. Luther, J. J. Berry, D. T. Moore, Enabling Flexible All-Perovskite Tandem Solar Cells. *Joule* **3**, 2193–2204 (2019).

28. D. Zhao, C. Chen, C. Wang, M. M. Junda, Z. Song, C. R. Grice, Y. Yu, C. Li, B. Subedi, N. J. Podraza, X. Zhao, G. Fang, R.-G. Xiong, K. Zhu, Y. Yan, Efficient two-terminal all-perovskite tandem solar cells enabled by high-quality low-bandgap absorber layers. *Nat. Energy* **3**, 1093–1100 (2018).

29. Z. Yang, Z. Yu, H. Wei, X. Xiao, Z. Ni, B. Chen, Y. Deng, S. N. Habisreutinger, X. Chen, K. Wang, J. Zhao, P. N. Rudd, J. J. Berry, M. C. Beard, J. Huang, Enhancing electron diffusion length in narrow-bandgap perovskites for efficient monolithic perovskite tandem solar cells. *Nat. Commun.* **10**, 4498 (2019).

30. J. W. Yoo, J. Jang, U. Kim, Y. Lee, S.-G. Ji, E. Noh, S. Hong, M. Choi, S. Il Seok, Efficient perovskite solar mini-modules fabricated via bar-coating using 2-methoxyethanol-based formamidinium lead tri-iodide precursor solution. *Joule* **5**, 2420–2436 (2021).

31. S. Jariwala, H. Sun, G. W. P. Adhyaksa, A. Lof, L. A. Muscarella, B. Ehrler, E. C. Garnett, D. S. Ginger, Local Crystal Misorientation Influences Non-radiative Recombination in Halide Perovskites. *Joule* **3**, 3048–3060 (2019).

32. Y. Zhao, P. Miao, J. Elia, H. Hu, X. Wang, T. Heumueller, Y. Hou, G. J. Matt, A. Osvet, Y.-T. Chen, M. Tarragó, D. de Ligny, T. Przybilla, P. Denninger, J. Will, J. Zhang, X. Tang, N. Li, C. He, A. Pan, A. J. Meixner, E. Spiecker, D. Zhang, C. J. Brabec, Strain-activated light-induced halide segregation in mixed-halide perovskite solids. *Nat. Commun.* **11**, 6328 (2020).

33. R. E. Beal, N. Z. Hagström, J. Barrier, A. Gold-Parker, R. Prasanna, K. A. Bush, D. Passarello, L. T. Schelhas, K. Brüning, C. J. Tassone, H. G. Steinrück, M. D. McGehee, M. F. Toney, A. F. Nogueira, Structural Origins of Light-Induced Phase Segregation in Organic-Inorganic Halide Perovskite Photovoltaic Materials. *Matter*. **2**, 207–219 (2020).

34. K. A. Bush, K. Frohna, R. Prasanna, R. E. Beal, T. Leijtens, S. A. Swifter, M. D. McGehee, Compositional Engineering for Efficient Wide Band Gap Perovskites with Improved Stability to Photoinduced Phase Segregation. *ACS Energy Lett.* **3**, 428–435 (2018).

35. L. A. Castriotta, M. Zendehdel, N. Yaghoobi Nia, E. Leonardi, M. Löffler, B. Paci, A. Generosi, B. Rellinghaus, A. Di Carlo, Reducing Losses in Perovskite Large Area Solar Technology: Laser Design Optimization for Highly Efficient Modules and Minipanels. *Adv. Energy Mater.* **2103420**, 2103420 (2022).

36. S. H. Reddy, F. Di Giacomo, A. Di Carlo, Low-Temperature-Processed Stable Perovskite Solar Cells and Modules: A Comprehensive Review. *Adv. Energy Mater.* **2103534**, 2103534 (2022).

37. R. Prasanna, T. Leijtens, S. P. Dunfield, J. A. Raiford, E. J. Wolf, S. A. Swifter, J. Werner, G. E. Eperon, C. de Paula, A. F. Palmstrom, C. C. Boyd, M. F. A. M. van Hest, S. F. Bent, G. Teeter, J. J. Berry, M. D. McGehee, Design of low bandgap tin–lead halide perovskite solar cells to achieve thermal, atmospheric and operational stability. *Nat. Energy* **4**, 939–947 (2019).

38. J. Yang, X. Liu, Y. Zhang, X. Zheng, X. He, H. Wang, F. Yue, S. Braun, J. Chen, J. Xu, Y. Li, Y. Jin, J. Tang, C. Duan, M. Fahlman, Q. Bao, Comprehensive understanding of heat-induced degradation of triple-cation mixed halide perovskite for a robust solar cell. *Nano Energy* **54**, 218–226 (2018).

39. L. Vesce, M. Stefanelli, J. P. Herterich, L. A. Castriotta, M. Kohlstädt, U. Würfel, A. Di Carlo, Ambient Air Blade-Coating Fabrication of Stable Triple-Cation Perovskite Solar Modules by Green Solvent Quenching. *Sol. RRL* **5**, 2100073 (2021).

40. R. Swartwout, R. Patidar, E. Belliveau, B. Dou, D. Beynon, P. Greenwood, N. Moody, D. DeQuilettes, M. Bawendi, T. Watson, V. Bulovic, Predicting Low Toxicity and Scalable Solvent Systems for High-Speed Roll-to-Roll Perovskite Manufacturing. *Sol. RRL* **6**, 2100567 (2021).

41. Q. Han, Y. Wei, R. Lin, Z. Fang, K. Xiao, X. Luo, S. Gu, J. Zhu, L. Ding, H. Tan, Low-temperature processed inorganic hole transport layer for efficient and stable mixed Pb-Sn low-bandgap perovskite solar cells. *Sci. Bull.* **64**, 1399–1401 (2019).

42. J. C. de Mello, H. F. Wittmann, R. H. Friend, An improved experimental determination of external photoluminescence quantum efficiency. *Adv. Mater.* **9**, 230–232 (1997).

43. R. D. J. Oliver, Y.-H. Lin, A. J. Horn, C. Q. Xia, J. H. Warby, M. B. Johnston, A. J. Ramadan, H. J. Snaith, Thermally Stable Passivation toward High Efficiency Inverted Perovskite Solar Cells. *ACS Energy Lett.* **5**, 3336–3343 (2020).

44. J. S. W. Godding, A. J. Ramadan, Y.-H. Lin, K. Schutt, H. J. Snaith, B. Wenger, Oxidative Passivation of Metal Halide Perovskites. *Joule* **3**, 2716–2731 (2019).

45. T. Kirchartz, J. A. Márquez, M. Stolterfoht, T. Unold, Photoluminescence-Based Characterization of Halide Perovskites for Photovoltaics. *Adv. Energy Mater.* **10**, 1904134 (2020).

46. Z. Yu, Z. Yang, Z. Ni, Y. Shao, B. Chen, Y. Lin, H. Wei, Z. J. Yu, Z. Holman, J. Huang, Simplified interconnection structure based on C60/SnO2-x for all-perovskite tandem solar cells. *Nat. Energy* **5**, 657–665 (2020).

47. Z. Yu, X. Chen, S. P. Harvey, Z. Ni, B. Chen, S. Chen, C. Yao, X. Xun, S. Xu, G. Yang, Y. Yan, J. J. Berry, M. C. Beard, J. Huang, Gradient Doping in Sn-Pb Perovskites by Barium Ions for Efficient Single-junction and Tandem Solar Cells. *Adv. Mater.* 2110351 (2022). DOI: 10.1002/adma.202110351

Acknowledgement:

Funding: This work was financially supported by the National Natural Science Foundation of China (61974063, 61921005, U21A2076), Natural Science Foundation of Jiangsu Province (BK20202008, BK20190315), Fundamental Research Funds for the Central Universities (0213/14380206; 0205/14380252), Frontiers Science Center for Critical Earth Material Cycling Fund (DLTD2109), Program for Innovative Talents and Entrepreneur in Jiangsu, and the Engineering and Physical Science Research Council, UK. Y.H. acknowledges the support from

the National University of Singapore (NUS) Presidential Young Professorship (R-279-000-617-133 and R-279-001-617-133). This work was authored in part by SERIS, a research institute at the NUS. SERIS is supported by NUS, the National Research Foundation Singapore (NRF), the Energy Market Authority of Singapore (EMA) and the Singapore Economic Development Board (EDB). **Author contributions:** H.T. conceived and directed the overall project. H.T. and H.J.S. supervised the research work. K.X. fabricated all the devices and conducted the characterization. M.Z. fabricated NBG perovskite films, R.D.J.O. and Y.-H.L. carried out PLQY measurement, Z.L. carried out GIWAXS characterization, X.L. helped on module encapsulation and carried out TPV measurement, H.L. and R.L. carried out SEM characterization, J.X. helped on the UV-vis absorption and SEM-EDX characterizations. Y.H., X.W. and J.L. assisted with data analyses. K.X., Y.-H.L., D.L., Y.H., H.J.S. and H.T. wrote the manuscript. All authors read and commented on the manuscript. **Competing interests:** H.T. and K.X. are inventors on a patent application related to this work filed by Nanjing University. H.J.S is a co-founder, CSO and a director of Oxford PV Ltd, a company commercializing perovskite PV. The other authors declare that they have no competing interests. **Data and materials availability:** All data are available in the main text or the supplementary materials.

Supplementary Materials:

Materials and Methods
Figures S1-38
Tables S1-6
References (*41-47*)
Movie S1-2

FIGURE CAPTIONS:

Fig. 1. Fabrication of $Cs_xFA_{1-x}PbI_{1.8}Br_{1.2}$ wide-bandgap perovskite films using blade coating. (**A**) Schematic illustration of gas-assisted blade coating. (**B** and **C**) SEM images and XRD patterns of $Cs_xFA_{1-x}PbI_{1.8}Br_{1.2}$ perovskite films. The scale bars in SEM images are 1 μm. (**D**) J-V curves of champion $Cs_xFA_{1-x}PbI_{1.8}Br_{1.2}$ PSCs. (**E**) QFLS calculated from the PLQY for the respective perovskite films and the perovskites with transport layer stacks investigated in the study. The Shockley-Queisser radiative limit and the experimental V_{oc} are plotted for each composition.

Fig. 2. Fabrication of all-perovskite tandem solar cells fully using scalable techniques. (**A**) Configuration schematic of an all-perovskite tandem device fabricated fully using scalable techniques. Processing technique for each layer is marked at left. (**B**) Cross-sectional SEM image of the all-perovskite tandem device. (**C**) J-V curves of the champion tandem solar cell (aperture area = 1.05 cm^2) deposited on 2.5 cm by 2.5 cm substrate. The inset shows the PCE distribution of 19 devices. (**D**) EQE curves of the champion device. The front and back subcells have integrated J_{sc} values of 15.6 and 16.6 mA cm^{-2}, respectively.

Fig. 3. All-perovskite tandem modules. (**A**) Structure schematic diagram of the series connected all-perovskite tandem module with CDB to prevent ion diffusion. (**B**) J-V curves of different module configurations. BCP: bathocuproine. (**C**) Relationship among fill factor, geometric fill factor, and efficiency of modules. (**D**) J-V curves of the champion all-perovskite tandem module. (Aperture area of 20.25 cm^2, 4 subcells in series) The insert is the front (left) and back (right) side photos of module. (**E**) Summary of publicly reported, independently certified PCEs of perovskite solar modules (aperture area $\geqslant$ 10 cm^2).

Fig.4. Stability of all-perovskite tandem solar modules. (**A**) Continuous MPP tracking of an encapsulated tandem module over 500 h under full simulated AM1.5G illumination (100 mW cm^{-2}, LED simulator) in ambient air with a humidity of 30-50%. (**B**) Thermal stability tracking of the tandem modules heated on a 85℃ hotplate in a N_2 glove box. (**C**) The Ag 3d XPS spectra of the

perovskite surfaces after peeling off the C_{60}/ALD-SnO_2/Ag stacks. The x-ray beam is located at the center of the exposed perovskite surface after peeling off the C_{60}/ALD-SnO_2/Ag stacks.

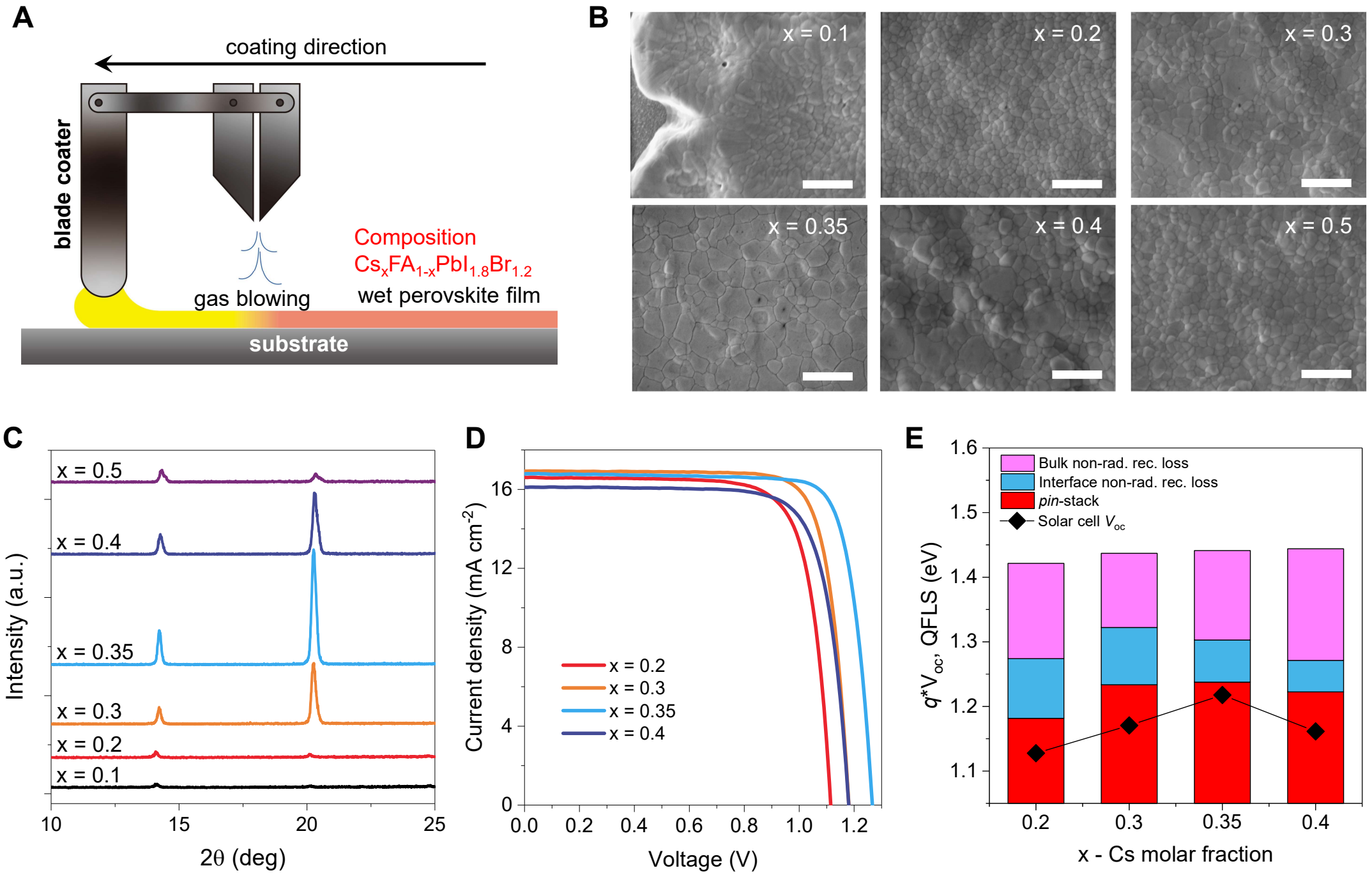
A
coating direction
blade coater
gas blowing
Composition
$Cs_xFA_{1-x}PbI_{1.8}Br_{1.2}$
wet perovskite film
substrate
B
x = 0.1
x = 0.2
x = 0.3
x = 0.35
x = 0.4
x = 0.5
C
x = 0.5
x = 0.4
x = 0.35
x = 0.3
x = 0.2
x = 0.1
Intensity (a.u.)
10
15
20
25
2θ (deg)
D
Current density (mA cm^{-2})
0
4
8
12
16
0.0
0.2
0.4
0.6
0.8
1.0
1.2
Voltage (V)
x = 0.2
x = 0.3
x = 0.35
x = 0.4
E
Bulk non-rad. rec. loss
Interface non-rad. rec. loss
pin-stack
Solar cell V_{oc}
q^*V_{oc}, QFLS (eV)
1.1
1.2
1.3
1.4
1.5
1.6
0.2
0.3
0.35
0.4
x - Cs molar fraction

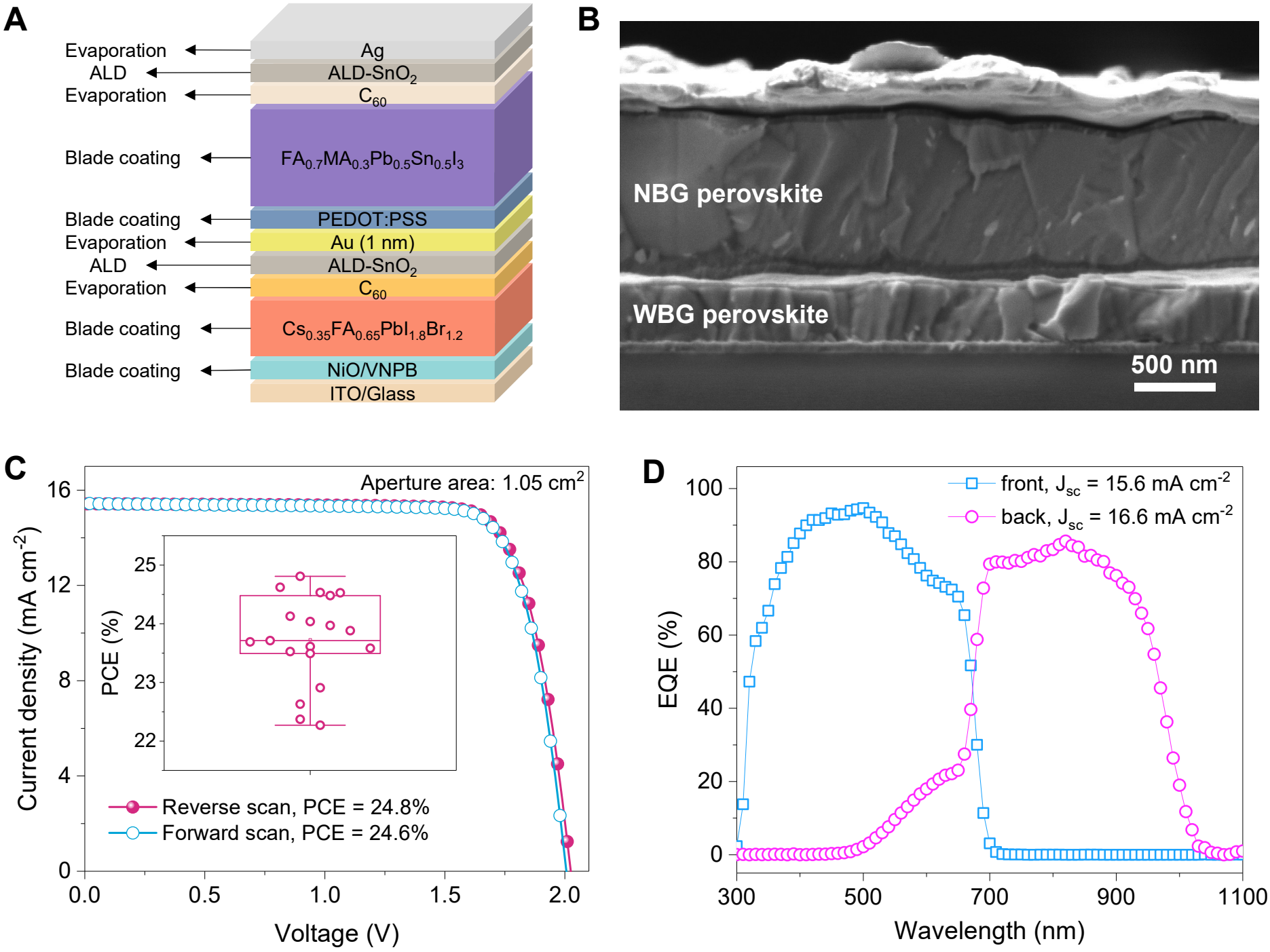
A
Evaporation
Ag
ALD
ALD-SnO2
Evaporation
C60
Blade coating
FA0.7MA0.3Pb0.5Sn0.5I3
Blade coating
PEDOT:PSS
Evaporation
Au (1 nm)
ALD
ALD-SnO2
Evaporation
C60
Blade coating
Cs0.35FA0.65PbI1.8Br1.2
Blade coating
NiO/VNPB
ITO/Glass
B
NBG perovskite
WBG perovskite
500 nm
C
Aperture area: 1.05 cm2
Current density (mA cm-2)
Voltage (V)
PCE (%)
Reverse scan, PCE = 24.8%
Forward scan, PCE = 24.6%
D
front, Jsc = 15.6 mA cm-2
back, Jsc = 16.6 mA cm-2
EQE (%)
Wavelength (nm)

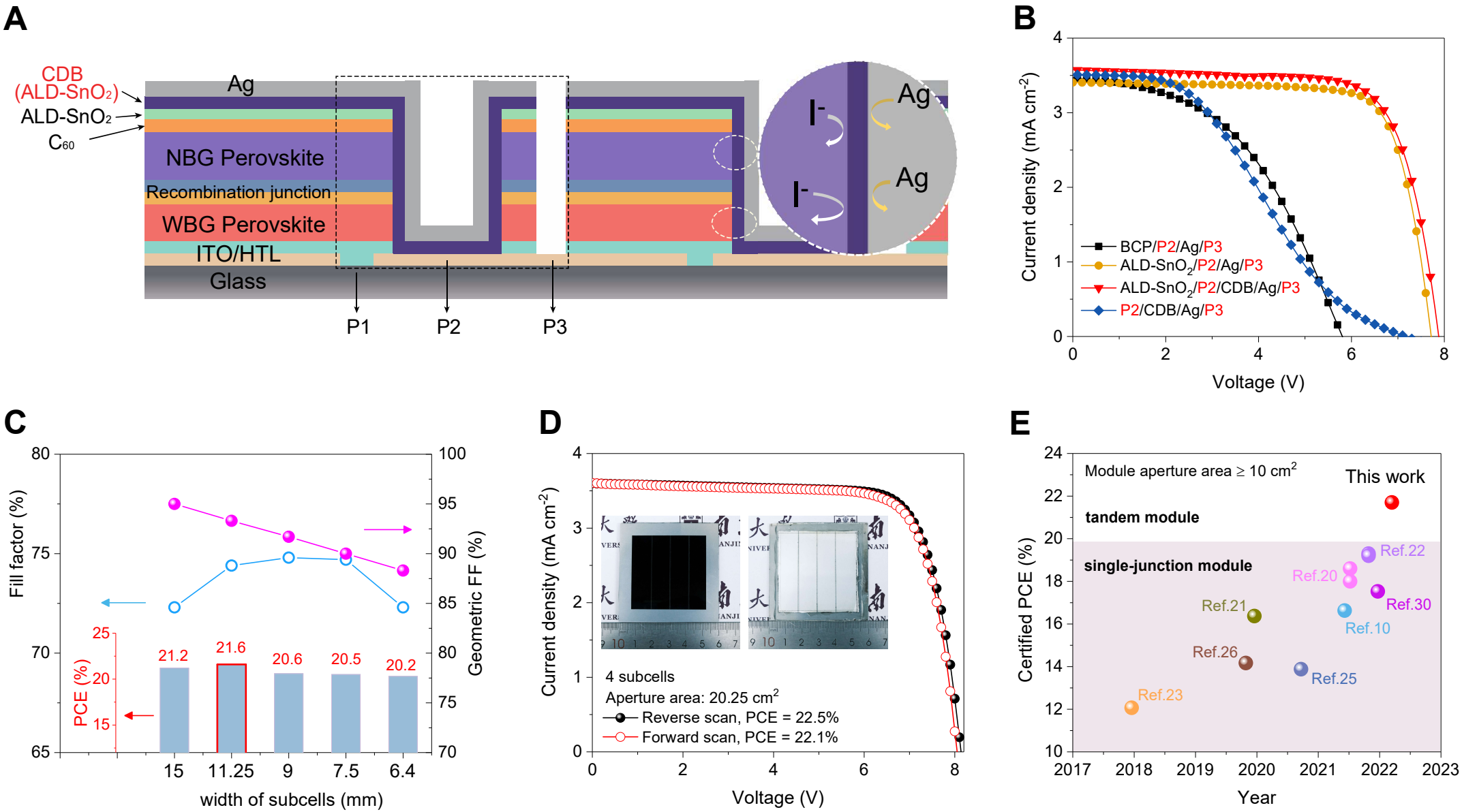
A
CDB
(ALD-SnO2)
ALD-SnO2
C60
Ag
NBG Perovskite
Recombination junction
WBG Perovskite
ITO/HTL
Glass
P1
P2
P3
I-
I-
Ag
Ag
B
Current density (mA cm-2)
Voltage (V)
BCP/P2/Ag/P3
ALD-SnO2/P2/Ag/P3
ALD-SnO2/P2/CDB/Ag/P3
P2/CDB/Ag/P3
C
Fill factor (%)
Geometric FF (%)
PCE (%)
21.2
21.6
20.6
20.5
20.2
15
11.25
9
7.5
6.4
width of subcells (mm)
D
Current density (mA cm-2)
Voltage (V)
4 subcells
Aperture area: 20.25 cm2
Reverse scan, PCE = 22.5%
Forward scan, PCE = 22.1%
E
Certified PCE (%)
Year
Module aperture area ≥ 10 cm2
This work
tandem module
single-junction module
Ref.22
Ref.20
Ref.30
Ref.21
Ref.10
Ref.26
Ref.25
Ref.23

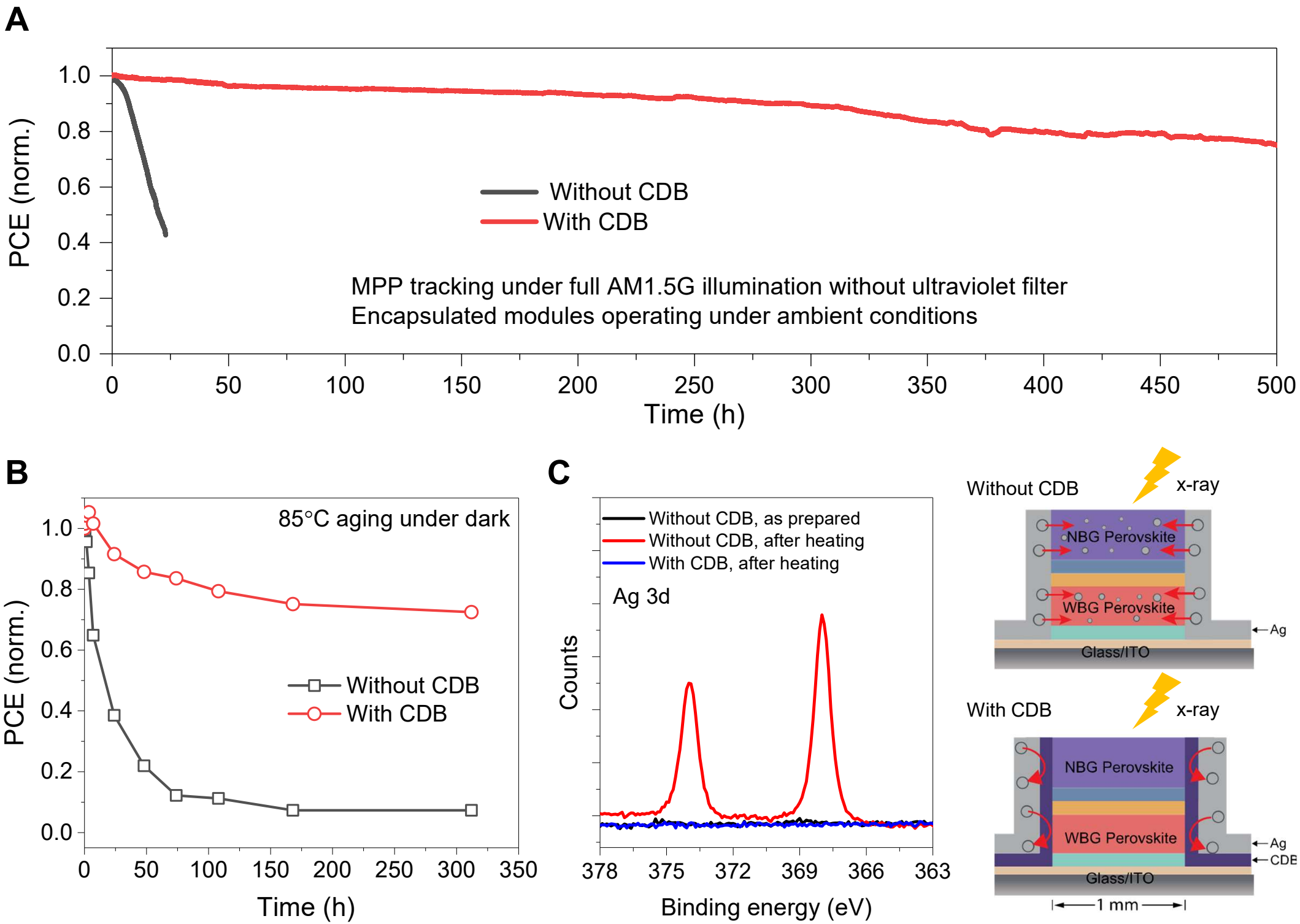
A
PCE (norm.)
Time (h)
Without CDB
With CDB
MPP tracking under full AM1.5G illumination without ultraviolet filter
Encapsulated modules operating under ambient conditions
B
85°C aging under dark
PCE (norm.)
Time (h)
Without CDB
With CDB
C
Without CDB, as prepared
Without CDB, after heating
With CDB, after heating
Ag 3d
Counts
Binding energy (eV)
Without CDB
x-ray
NBG Perovskite
WBG Perovskite
Ag
Glass/ITO
With CDB
x-ray
NBG Perovskite
WBG Perovskite
Ag
CDB
Glass/ITO
1 mm

Science
AAAS

Supplementary Materials for

Scalable processing for realizing 21.7% efficient all-perovskite tandem solar modules

Ke Xiao[1,5], Yen-Hung Lin[2], Mei Zhang[1], Robert D. J. Oliver[2], Xi Wang[3,4], Zhou Liu[1], Xin Luo[1,5], Jia Li[4], Donny Lai[4], Haowen Luo[1], Renxing Lin[1], Jun Xu[5], Yi Hou[3,4], Henry J. Snaith[2]*, and Hairen Tan[1]*

[1]National Laboratory of Solid State Microstructures, Jiangsu Key Laboratory of Artificial Functional Materials, College of Engineering and Applied Sciences, Nanjing University, Nanjing 210093, China.

[2]Clarendon Laboratory, Department of Physics, University of Oxford, Oxford OX1 3PU, UK.

[3]Department of Chemical and Biomolecular Engineering, National University of Singapore, 4 Engineering Drive 4, 117585 Singapore

[4]Solar Energy Research Institute of Singapore (SERIS), National University of Singapore, 7 Engineering Drive 1, 117574, Singapore.

[5]School of Electronics Science and Engineering, Nanjing University, Nanjing 210093, China.

*Correspondence to: hairentan@nju.edu.cn (H.T.); henry.snaith@physics.ox.ac.uk (H.J.S)

This PDF file includes:

Other Supplementary Materials for this manuscript include the following:

Materials and Methods

Materials

All materials were used as received without further purification. The organic halide salts (FAI, MAI and phenylethylammonium iodide (PEAI) with purity of >99%) were purchased from GreatCell Solar Materials. PEDOT-PSS aqueous solution (Al 4083) was purchased from Heraeus Clevios. PbI_2 (99.99%, trace metals basis) and $PbBr_2$ (99.99%, trace metals basis) were purchased from TCI. SnI_2 (99.999%, trace metals basis) was purchased from Alfa Aesar. SnF_2 (99%), tin powders (<150 μm, 99.5%), CsI (99.999%), DMF (99.8% anhydrous), DMSO (99.9% anhydrous), formamidine sulfinic acid (FSA, ≥98%), chlorobenzene (99.8% anhydrous) were purchased from Sigma-Aldrich. The C_{60} was purchased from Nano-C. N4,N4′-di(naphthalen-1-yl)-N4,N4′-bis(4-vinylphenyl) biphenyl-4,4′-diamine (VNPB, >95%) was purchased from Lumtec.

Perovskite precursor solution

Wide-bandgap $Cs_xFA_{1-x}PbI_{1.8}Br_{1.2}$ perovskite: The precursor solution (1.4 M) was prepared in mixed solvents of DMF and DMSO with a volume ratio of 4:1. The molar ratios for CsI/FAI and PbI_2/$PbBr_2$ were x:(1-x) and 0.4:0.6, respectively. The molar ratio of (CsI + FAI)/(PbI_2 + $PbBr_2$) was 1:1. PEAI (0.5 mol% relative to PbX_2) was added in the precursor solution as the additive. The precursor solution was stirred at room temperature overnight, then filtered through a 0.22 μm polytetrafluoroethylene (PTFE) membrane before making the perovskite films.

Narrow-bandgap $FA_{0.7}MA_{0.3}Pb_{0.5}Sn_{0.5}I_3$ perovskite: The precursor solution (2.4 M) was prepared in mixed solvents of DMF and DMSO with a volume ratio of 9:1. The molar ratios for FAI/MAI and PbI_2/SnI_2 were 0.7:0.3 and 0.5:0.5, respectively. The molar ratio of (FAI + MAI)/(PbI_2 + SnI_2) was 1:1. SnF_2 (10 mol% relative to SnI_2) was added in the precursor solution. FSA (0.2 mol%) as the additive and tin powders (5 mg ml^{-1}) as the antioxidant were added to the precursor solution. The precursor solution was stirred at room temperature for 2 h. The precursor solution was filtered through a 0.22 μm PTFE membrane before making the perovskite films.

All-perovskite tandem solar cell fabrication

Patterned ITO glass substrates were sequentially cleaned using ultrasonication with acetone and isopropanol for 30 min, respectively. NiO nanocrystals were synthesized according to previous reports(*41*). NiO nanocrystal (5 mg ml^{-1} in deionized water) was blade coated onto ITO glass substrates at a speed of 10 mm s^{-1}. The N_2 knife worked at 10 psi during blade coating. The gap between the blade coater and ITO substrate was 200 μm. The substrates were transferred onto a hotplate and annealed at 100 °C for 10 min in air. Then VNPB (0.5 mg ml^{-1} in chlorobenzene) was blade coated onto substrates at a speed of 10 mm s^{-1} and annealed at 150 °C for 10 min in air. The wide-bandgap perovskite ($Cs_xFA_{1-x}PbI_{1.8}Br_{1.2}$) precursor solution was blade coated on the NiO/VNPB-covered ITO glass substrates with a gap of 200 μm at a movement speed of 5 mm s^{-1} in a N_2 glove box (H_2O < 0.01 ppm, O_2 < 0.01 ppm). The N_2 knife worked at 60 psi during blade coating. After that, the perovskite films were annealed at 105 °C for 20 min. After cooling to room temperature, the substrates were transferred to the evaporation system, and a 20-nm-thick C_{60} film was subsequently deposited on top by thermal evaporation (Beijing Technol Science Co., Ltd) at a rate of 0.2 Å s^{-1}. The substrates were then transferred to the ALD system (Veeco Savannah S200) to deposit 20 nm SnO_2 at low temperatures (typically 100 °C) using precursors of tetrakis(dimethylamino) tin(iv) (99.9999%, Nanjing Ai Mou Yuan Scientific Equipment) and deionized water. After ALD deposition, the substrates were transferred back to the thermal evaporation system to deposit an ultrathin layer of Au clusters (~1 nm) on ALD-SnO_2. PEDOT-PSS was diluted using deionized water for 1:1

and then blade-coated on the top of SnO_2-protected front cells. The blade coater moved at a speed of 10 mm s^{-1} and the N_2 knife worked at 10 psi during blade coating. Then the substrates were transferred onto a hotplate and annealed at 100 °C for 20 min in air. After the substrates had cooled, we immediately transferred the substrates to a nitrogen-filled glovebox for the deposition of narrow-bandgap perovskite films. The narrow-bandgap perovskite ($FA_{0.7}MA_{0.3}Pb_{0.5}Sn_{0.5}I_3$) precursor solution was blade coated on the substrates with a gap of 200 μm at a movement speed of 5 mm s^{-1}. The N_2 knife worked at 60 psi during blade coating. After that, the perovskite films were annealed at 100 °C for 10 min. Then, 20 nm C_{60} film was subsequently deposited on top by thermal evaporation at a rate of 0.2 Å s^{-1}. The ALD-SnO_2 layer (~15 nm) was deposited after C_{60} deposition at low temperatures (typically 70 °C) to avoid any damage to the Pb-Sn perovskite absorber layer. Finally, 100 nm Ag films as electrode were deposited by thermal evaporation at the rates of 1.0 Å s^{-1}.

Module fabrication

As illustrated in fig. S23, the modules were fabricated on the prepatterned 6 cm-by-6 cm ITO glass substrates using laser scribing (P1 width 50 μm, 20 W, 1064 nm, 20 kHz), following the same procedures as the solar cells before electrode. The fabricated modules typically have 3 to 7 subcells, with corresponding width of 15 mm, 11.25 mm, 9 mm, 7.5 mm, 6.4 mm, respectively. The P2 were mechanically scribed using a needle pen in ambient air. After P2, the modules were transferred to the ALD system. The CDB (ALD-SnO_2, ~10 nm with 100 ALD cycles) was deposited after P2 as interdiffusion barrier. Finally, 250 nm Ag films as electrode were deposited by thermal evaporation at the rates of 1.0 Å s^{-1}. The P3 was also mechanically scribed in ambient air. The width of dead area was about 0.75 mm, as shown in fig. S26.

Device characterization

For single-junction solar cells, the J-V characteristics were measured using a Keithley 2400 sourcemeter under the illumination of the solar simulator (EnliTech, Class AAA) at a light intensity of 100 mW cm^{-2} as checked with a calibrated reference solar cell (KG-5 and KG-0 reference cells were used for the measurements of WBG and NBG perovskite solar cells, respectively). Unless otherwise stated, the J-V curves were all measured in a nitrogen-filled glovebox with a scanning rate of 100 mV s^{-1} (voltage steps of 10 mV and a delay time of 100 ms). The active area was determined by the aperture shade masks (0.049, 1.05 cm^2) placed in front of the solar cells. EQE measurements were performed in ambient air using a QE system (EnliTech) with monochromatic light focused on a device pixel and a chopper frequency of 20 Hz. For tandem solar cells and modules, the J-V characteristics were carried out under the illumination of a dual-lamp simulator (SAN-EI ELECTRIC, XHS-50S1) at a light intensity of 100 mW cm^{-2} as checked with calibrated reference solar cells (KG-0). The spectrum from the simulator was finely tuned to ensure that spectral mismatch was within 3% for both subcells. EQE measurements were performed in ambient air, and the bias illumination from highly bright LEDs with emission peaks of 850 and 460 nm was used for the measurements of the front subcells and back subcells, respectively. The active area was determined by the aperture shade mask (20.25 cm^2) placed in front of the modules.

Stability tests of solar cells

The operational stability tests were carried out under full AM1.5G illumination (multi-colored LED solar simulator, 100 mW cm^{-2}) using a home-build LabVIEW-based MPP tracking system using a ‘perturb and observe’ method in ambient conditions with humidity of 30-50%. The modules were encapsulated with a cover glass and ultraviolet epoxy (Three Bond), which was cured under an ultraviolet light-emitting diode lamp (peak emission at 365 nm) for 3 min. The

environmental temperature was kept at around 25 °C (varied between 21-26 °C). The module temperature increased to 35-50 °C under illumination as no active cooling was implemented to the measurement stage (fig. S38). The dark long-term shelf stability assessments of modules (with encapsulation) were carried out by repeating the J-V characterizations over various times, and the devices were stored in ambient conditions with humidity of 30-50%. The thermal stability tests of modules (with encapsulation) were carried out by repeating the J-V characterizations over various times. The modules were heated in a N_2 glove box.

XPS characterization

Sample preparation: The same processes as all-perovskite tandem solar cell fabrication above until 20 nm C_{60} film deposited on the top of NBG perovskites. The ALD-SnO_2 layer (~15 nm) was deposited after C_{60} deposition. For CDB devices, P2 was scribed by laser (10 W, 1064 nm, 20 kHz) with an interval of 1 mm. 10-nm CDB layer was deposited using ALD for CDB devices after P2 process. For control (without CDB) devices, P2 was scribed same as above mentioned after both 15-nm ALD-SnO_2 layer and 10-nm CDB layer deposition sequentially. Finally, 250 nm Ag film as electrode was deposited by thermal evaporation. These devices were preheated at 85 °C overnight in N_2 glove box before XPS scoping. XPS analysis was carried out using the Thermo Scientific Al K-Alpha XPS system with energy steps of 0.1 eV.

Photoluminescence quantum yield (PLQY)

The PLQY samples were prepared using the following architectures: glass/perovskite for neat perovskite materials, and glass/ITO/NiO/VNPB/perovskite/C_{60} for *pin*-stacks. PLQY measurements were performed following the procedure developed by de Mello et al. (*42*) and as we have reported previously e.g. (*43*, *44*). In brief, the samples were placed in an integrated sphere (Newport, 70682NS) and photoexcited by a 405 nm continuous wave laser. The signal was coupled into a fibre and collected by an Ocean Optics QEPro spectrometer. The integrating sphere and fibre were calibrated using a lamp of known spectrum (Ocean Insight, HL-3P-INT-CAL). The illumination intensity was modulated with neutral density (ND) filters to achieve a near 1-sun equivalent photon flux at a bandgap of 1.8 eV (*45*).

GIWAXS characterization

The grazing-incidence X-ray scattering (GI-XRD) data were recorded using an Xeuss 3.0 system. The photon energy was 9.24 keV (wavelength = 1.3414Å), and the incident angles are 1°. The diffracted X-rays were collected by a Eiger 2R 1M detector at a distance of 2000 mm.

Other characterizations

Scanning electron microscopy images were obtained using a Hitachi S8100 microscope with an accelerating voltage of 2 kV. X-ray diffraction patterns were collected using a Rigaku MiniFlex 600 diffractometer equipped with a NaI scintillation counter and using monochromatized Cu-Kα radiation (λ = 1.5406 Å). Optical absorption measurements were carried out in a Lambda 950 ultraviolet-visible spectrophotometer. Transient photovoltage decays were measured on a homemade system. A 540 nm green light-emitting diode was used to modulate the V_{oc} with a constant light bias, and the repetition rate was set to 2,000 Hz. A white light-emitting diode was illuminated on the active area of the solar cell under study for the constant light bias. The intensity of the pulsed illumination was set in a way that the modulated V_{oc} was ~10 mV to ensure a perturbation regime. The open-circuit voltage transient, induced by the light perturbation, was measured with a digital oscilloscope set to an input impedance of 1 MΩ. The charge recombination lifetime was fitted by a single exponential decay. Photoluminescence (PL) was measured using a FLS980 fluorescence spectrometer (Edinburgh Instruments) with an excitation wavelength of 405 nm. Atomic force microscope

(AFM) images were measured by Oxford. Scanning electron microscopy Energy Dispersive Spectrometer (SEM-EDS) was imaged by an energy dispersive spectrometer (Oxford) attached scanning electron microscopy (Zeiss, Sigma) with an accelerating voltage of 15 kV.

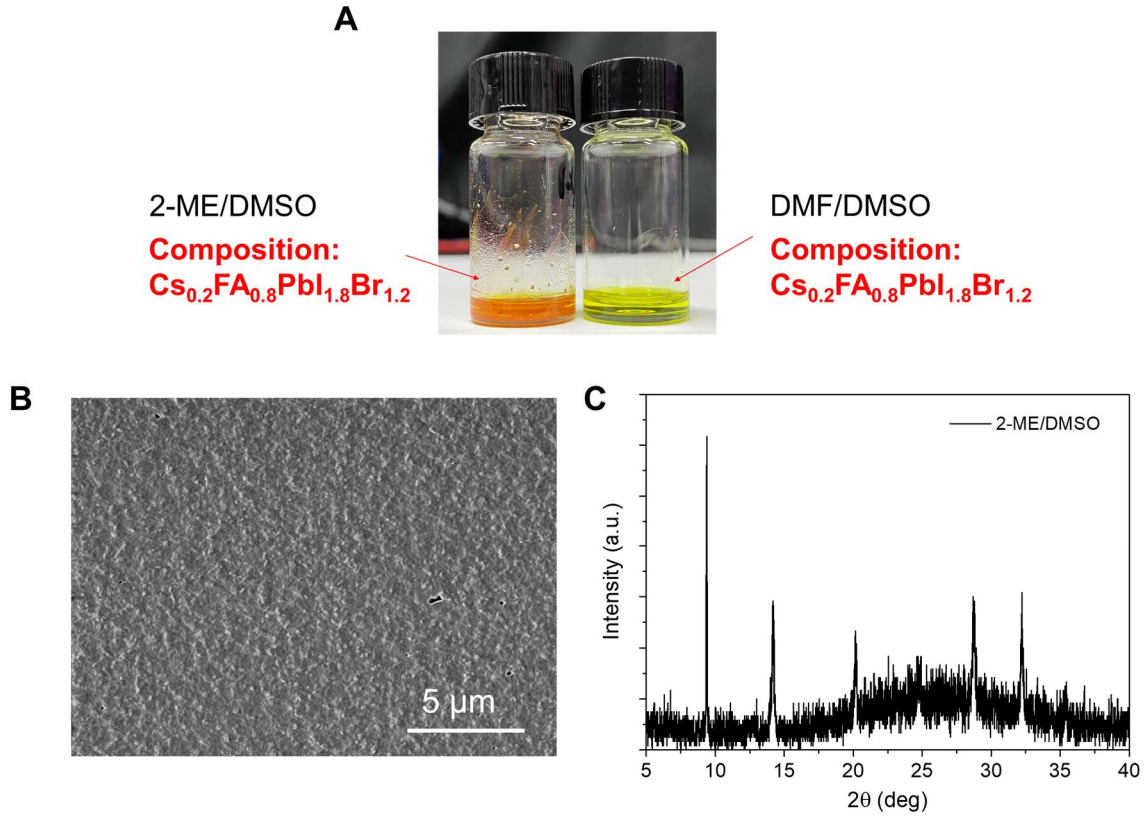

Fig. S1. Solvent engineering of $Cs_{0.2}FA_{0.8}PbI_{1.8}Br_{1.2}$ perovskite by gas-assisted blade coating. (**A**) Digital photo of $Cs_{0.2}FA_{0.8}PbI_{1.8}Br_{1.2}$ precursor ink with mixed 2-methoxyethanol (2-ME)/DMSO and mixed DMF/DMSO as solvent. 2-ME/DMSO precursor ink is prepared by mixing $CsPbI_{1.8}Br_{1.2}$ in DMSO and $FAPbI_{1.8}Br_{1.2}$ in 2-ME. The orange precipitate appears after mixing two clear precursor inks for 2 min. (**B**) SEM image and (**C**) XRD pattern of the $Cs_{0.2}FA_{0.8}PbI_{1.8}Br_{1.2}$ perovskite film prepared by 2-ME/DMSO mixed precursor using the liquid supernatant.

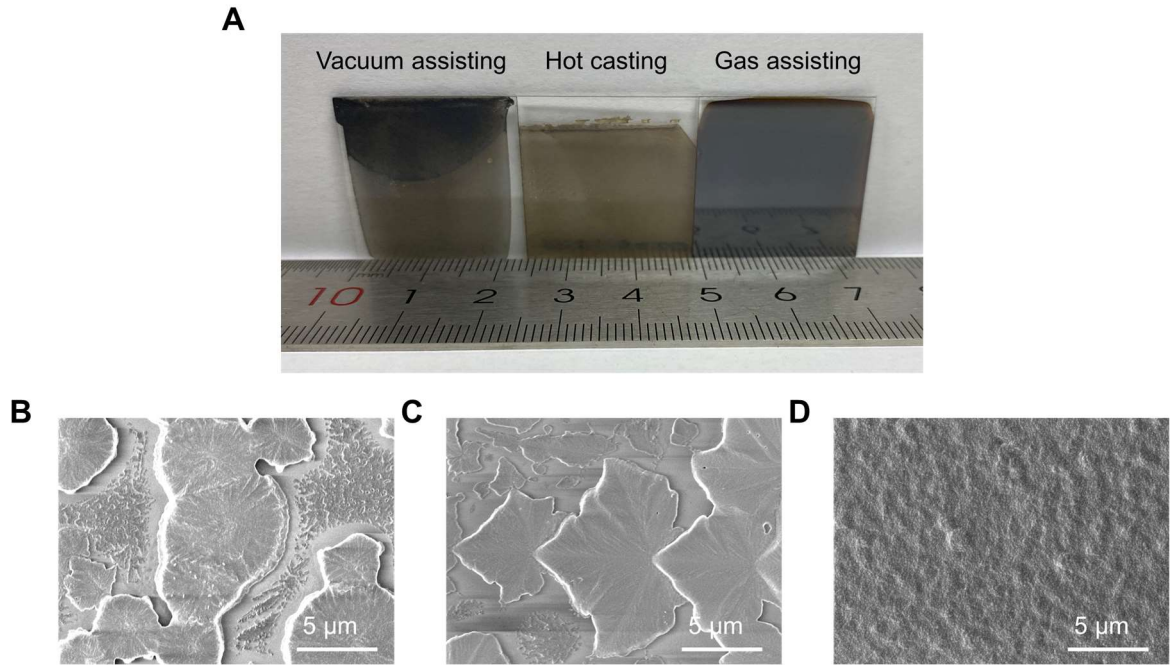

Fig. S2. Blade coated perovskite films ($Cs_{0.2}FA_{0.8}PbI_{1.8}Br_{1.2}$) via various crystallization assisted methods. (**A**) Digital photo of the perovskite films by blade coating on the 2.5 cm-by-2.5 cm substrates. For vacuum-assisted blade coating, as the precursor solution spread onto the substrate by blade coating, the wet perovskite film was transferred into a vacuum chamber, which was pumped to 1000 Pa in 15 s and stayed at the pressure for 1 min. For hot casting, precursor ink was dripped onto the ITO substrate, which was set on a hot plate at 110°C, and then swiped linearly by a blade coater at a speed of 5 mm s^{-1}. For gas-assisted blade coating, see the method section above mentioned. SEM images of the perovskite film prepared by (**B**) vacuum assisted blade coating, (**C**) hot casting blade coating and (**D**) gas-assisted blade coating.

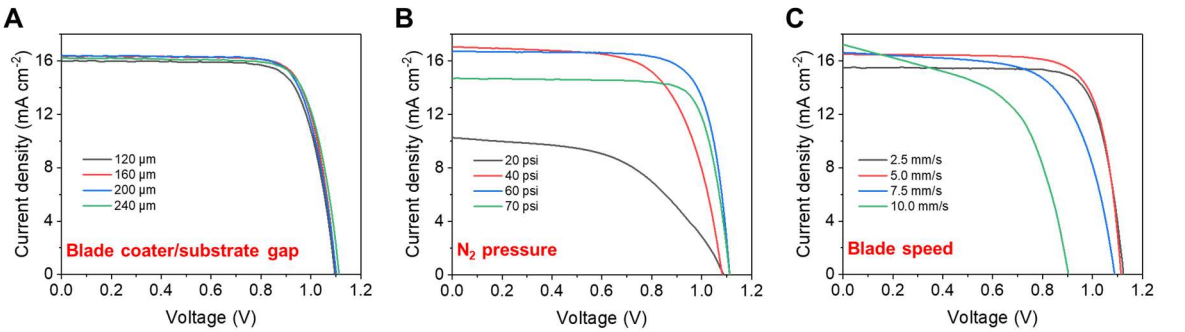

	V_{oc} (V)	J_{sc} (mA cm^{-2})	FF (%)	PCE (%)
120 μm	1.096	16.0	76.3	13.4
160 μm	1.101	16.3	77.8	14.0
200 μm	1.101	16.4	76.8	13.9
240 μm	1.113	16.2	77.0	13.9

	V_{oc} (V)	J_{sc} (mA cm^{-2})	FF (%)	PCE (%)
20 psi	1.089	10.3	52.0	5.8
40 psi	1.082	17.0	66.0	12.1
60 psi	1.112	16.7	76.5	14.2
70 psi	1.112	14.7	78.8	12.8

	V_{oc} (V)	J_{sc} (mA cm^{-2})	FF (%)	PCE (%)
2.5 mm/s	1.124	15.5	78.5	13.7
5.0 mm/s	1.115	16.5	76.5	14.1
7.5 mm/s	1.089	16.6	65.4	11.8
10 mm/s	0.904	17.2	54.6	8.5

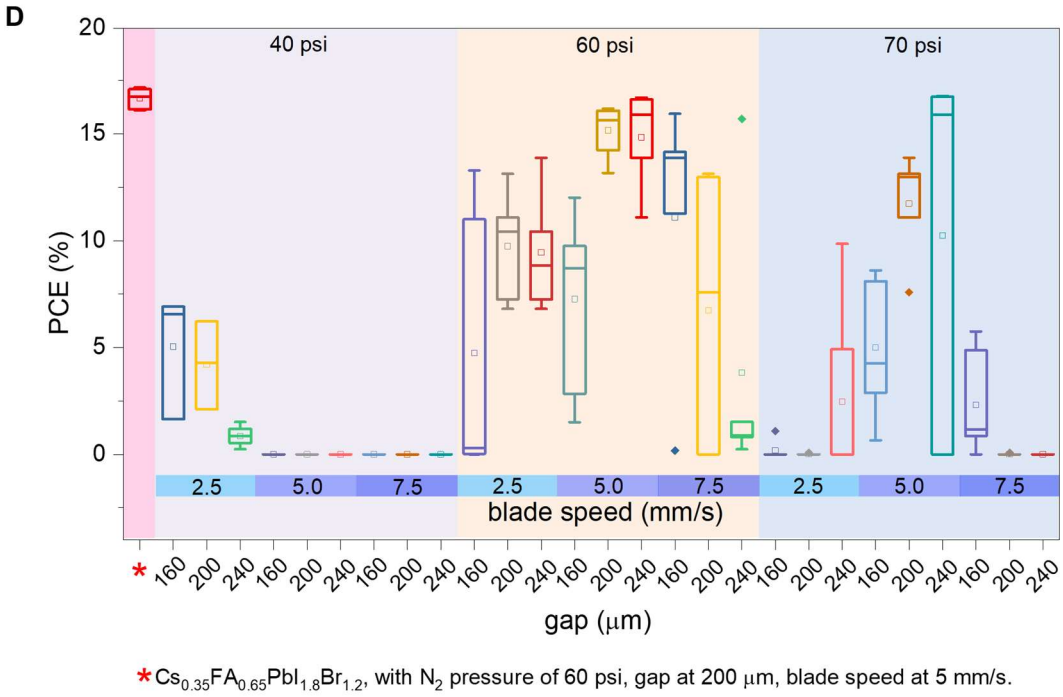

Fig. S3. Parameter optimization of the blade-coated $Cs_{0.2}FA_{0.8}PbI_{1.8}Br_{1.2}$ perovskite solar cells. (**A**) J-V curves of the WBG PSCs with varied gaps between blade coater and substrate. The blade speed is 5 mm/s and the N_2 knife worked at 60 psi. (**B**) J-V curves of the WBG PSCs with varied gas pressure during blade coating. The gap between blade coater and substrate is 200 μm and the blade speed is 5 mm/s. (**C**) J-V curves of the WBG PSCs with varied blade speed. The gap between blade coater and substrate is 200 μm and the N_2 knife worked at 60 psi. (**D**) A parameter space of the $Cs_{0.2}FA_{0.8}PbI_{1.8}Br_{1.2}$ perovskite films with various N_2 pressure, blade speed and gap between blade coater and substrate.

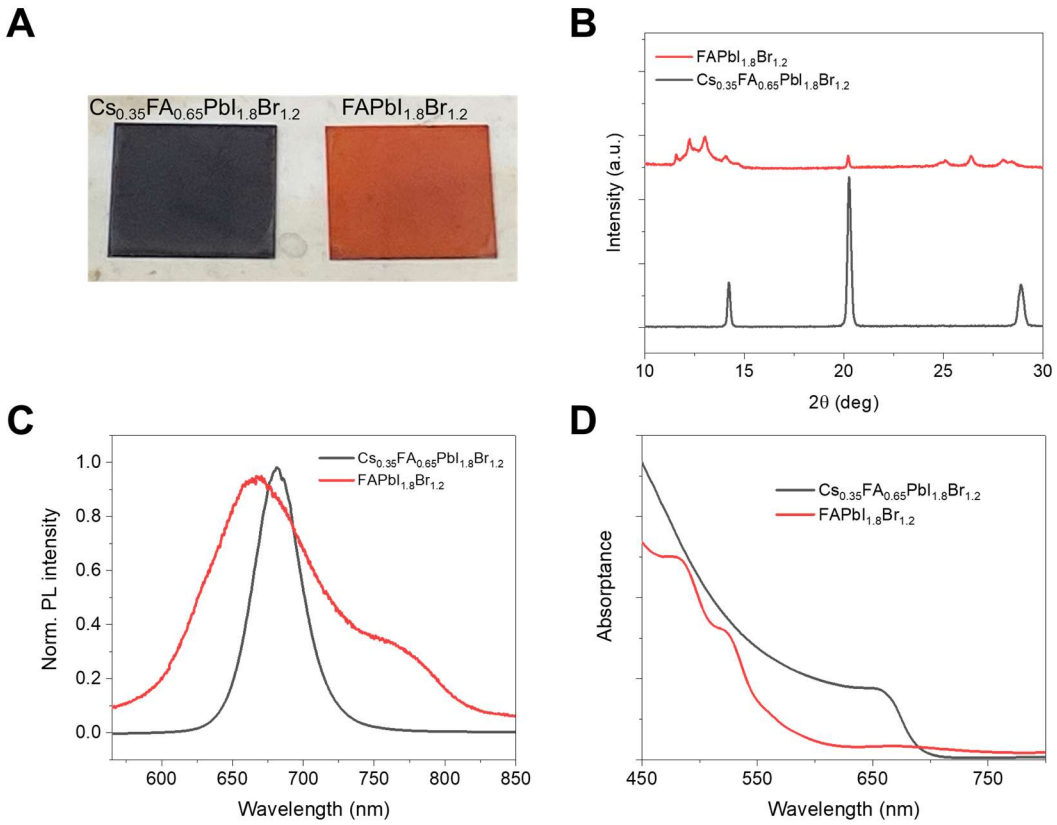

Fig S4. Comparison of the ~1.8-eV perovskites ($APbI_{1.8}Br_{1.2}$) with or without Cs. (**A**) Digital photo, (**B**) XRD patterns, (**C**) normalized PL spectra and (**D**) UV-Vis spectra of the $Cs_{0.35}FA_{0.65}PbI_{1.8}Br_{1.2}$ and $FAPbI_{1.8}Br_{1.2}$ perovskite films. The $FAPbI_{1.8}Br_{1.2}$ films exhibited an obvious non-perovskite δ phase.

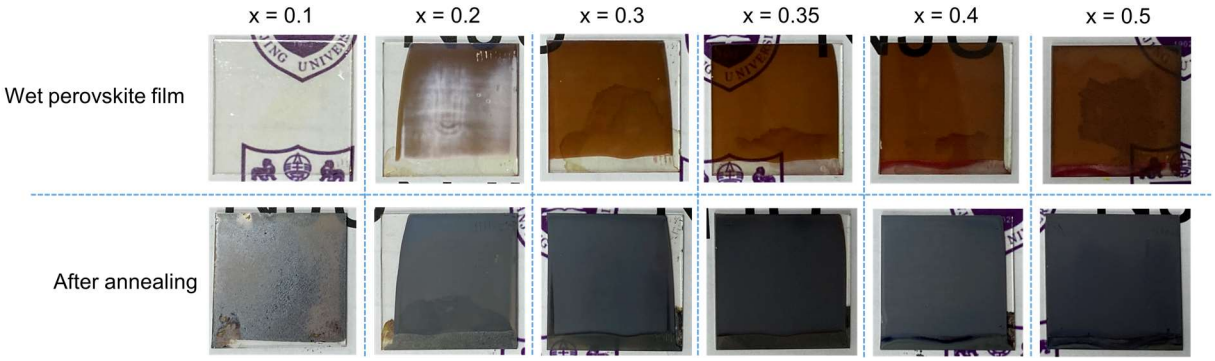

Fig. S5. Digital photos of the $Cs_xFA_{1-x}PbI_{1.8}Br_{1.2}$ perovskite films. Above row shows the photos of blade coated wet perovskite films just after gas blowing. Below row shows the corresponding wet perovskite films after 100°C annealing for 10 min.

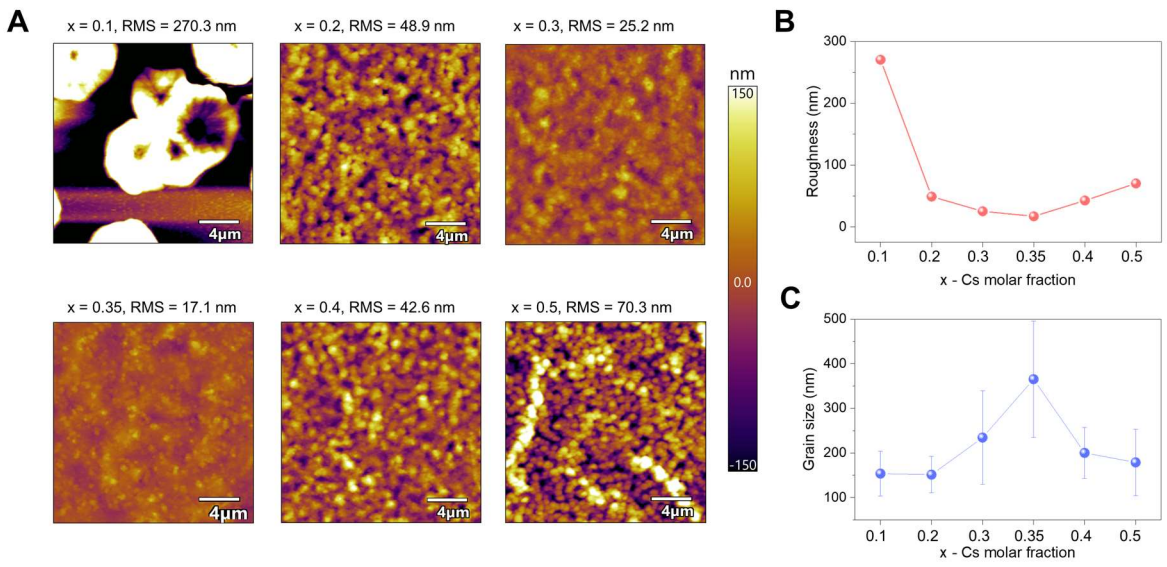

Fig. S6. Surface morphology of $Cs_xFA_{1-x}PbI_{1.8}Br_{1.2}$ perovskite films. (**A**) Atomic force microscopy (AFM) images of $Cs_xFA_{1-x}PbI_{1.8}Br_{1.2}$ perovskite films. (**B**) corresponding surface roughness summarized from AFM images. (**C**) grain size statistics of $Cs_xFA_{1-x}PbI_{1.8}Br_{1.2}$ perovskite films from SEM images in Fig. 1B.

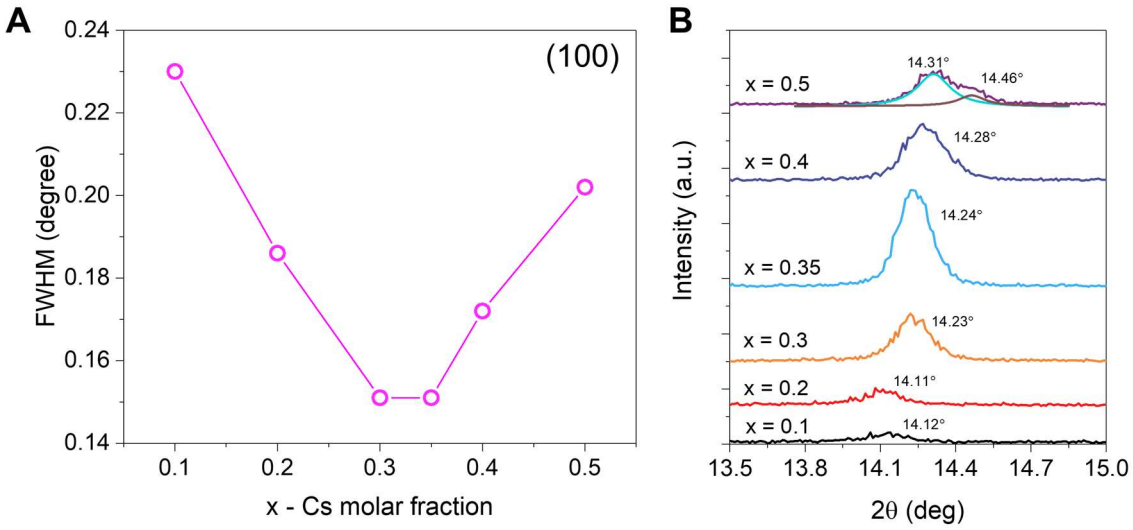

Fig. S7. XRD characteristics. (**A**) Full width at half-maximum (FWHM) of the (100) peak at 14.24°. (**B**) Part of the XRD pattern cut from Fig. 1C. An obvious peak splitting is observed for the composition of $Cs_{0.5}FA_{0.5}PbI_{1.8}Br_{1.2}$.

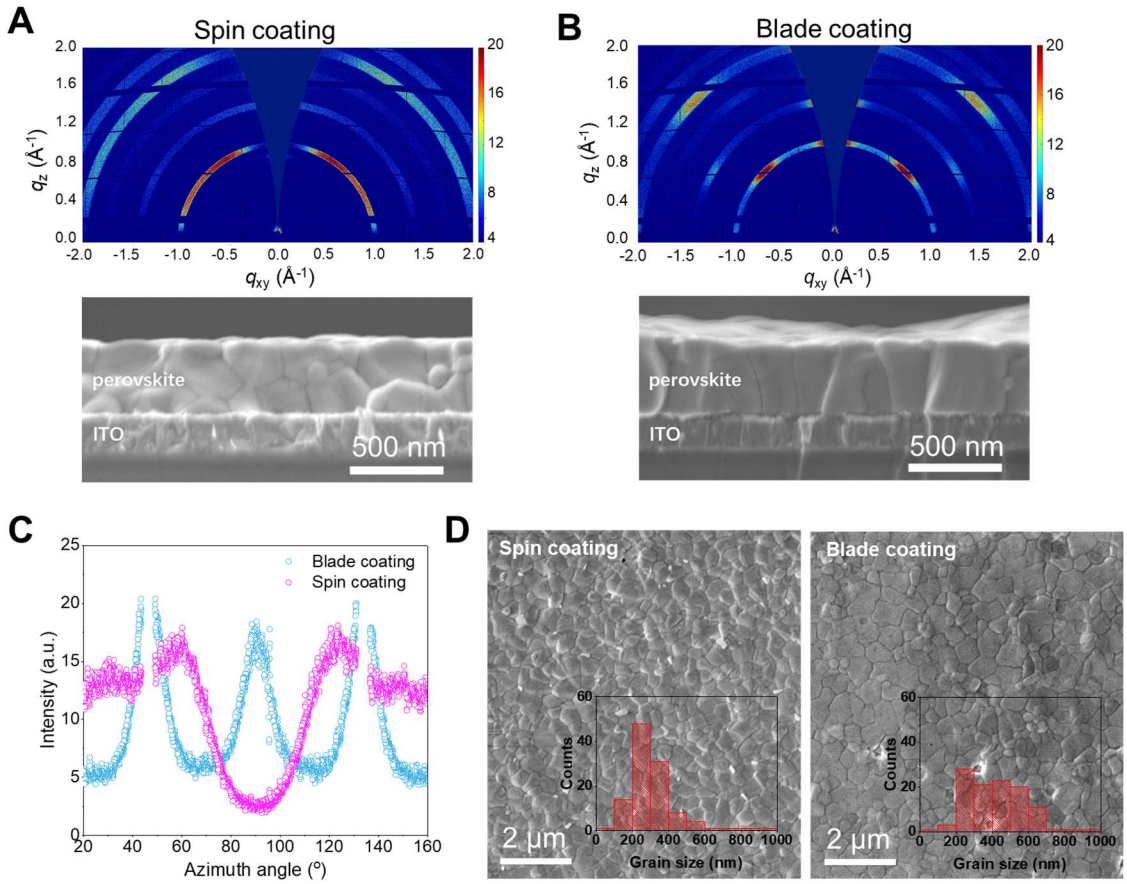

Fig. S8. Film characteristics of the spin-coated $Cs_{0.2}FA_{0.8}PbI_{1.8}Br_{1.2}$ perovskite film and blade-coated $Cs_{0.35}FA_{0.65}PbI_{1.8}Br_{1.2}$ perovskite film. 2D GIWAXS and Cross-sectional SEM images of (**A**) the spin-coated $Cs_{0.2}FA_{0.8}PbI_{1.8}Br_{1.2}$ perovskite film and (**B**) the blade-coated $Cs_{0.35}FA_{0.65}PbI_{1.8}Br_{1.2}$ perovskite film. (**C**) Integrated azimuth angle at 14.24° (100) from GIWAXS pattern in figs. S7A and S7B. (**D**) Top-view SEM images of the spin-coated $Cs_{0.2}FA_{0.8}PbI_{1.8}Br_{1.2}$ perovskite film (left) and the blade-coated $Cs_{0.35}FA_{0.65}PbI_{1.8}Br_{1.2}$ perovskite film (right). The average grain size of the spin-coated $Cs_{0.2}FA_{0.8}PbI_{1.8}Br_{1.2}$ perovskite film and the blade-coated $Cs_{0.35}FA_{0.65}PbI_{1.8}Br_{1.2}$ perovskite film are 290 nm and 380 nm, respectively.

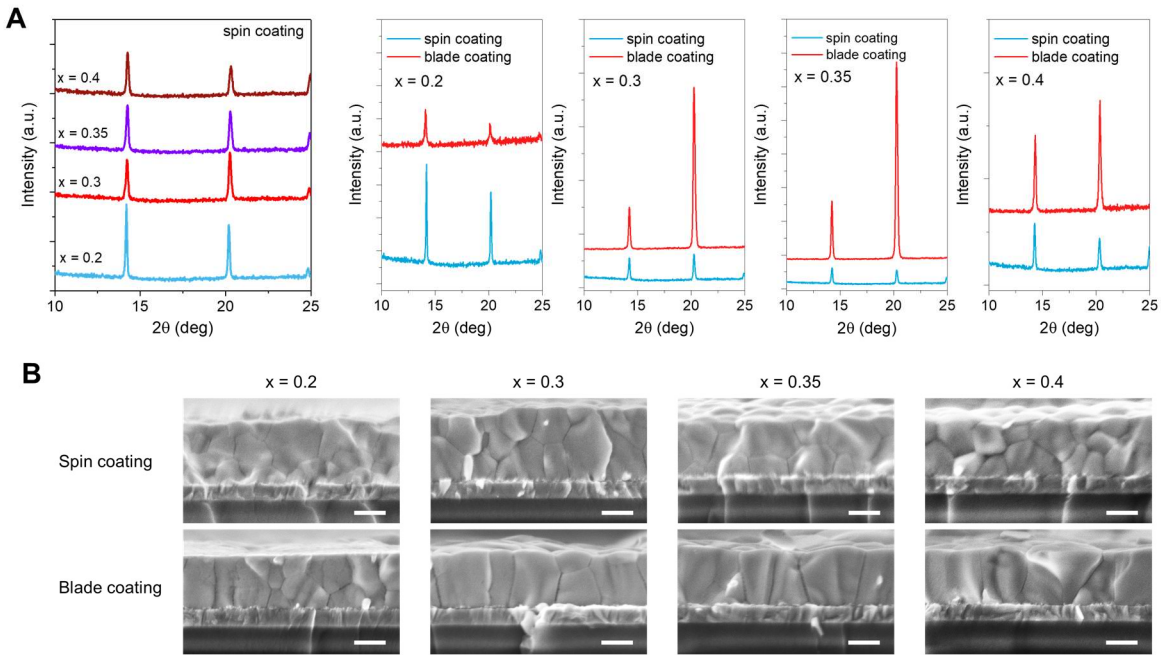

Fig. S9. Film characterization. (**A**) XRD patterns and (**B**) cross-sectional SEM images of $Cs_xFA_{1-x}PbI_{1.8}Br_{1.2}$ (x = 0.2~0.4) perovskite films prepared by spin coating and blade coating. The scale bars for **B** are 200 nm.

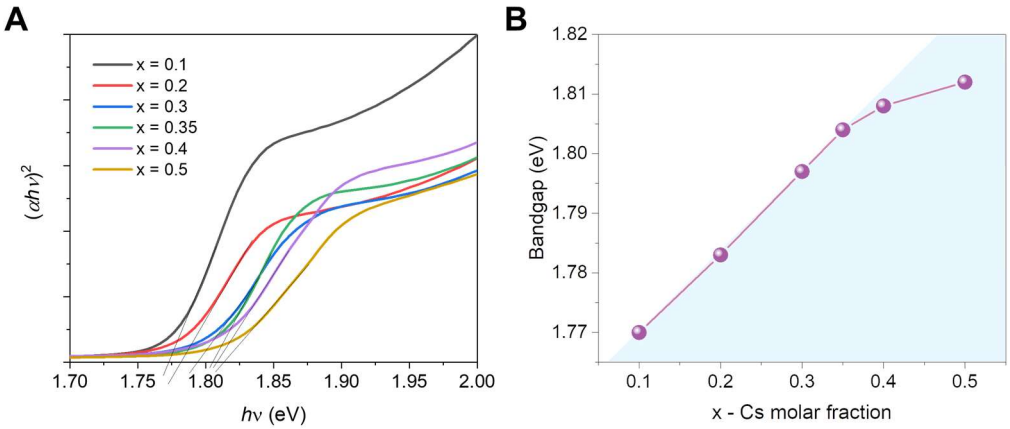

Fig. S10. Optical bandgap of the blade-coated $Cs_xFA_{1-x}PbI_{1.8}Br_{1.2}$ perovskite film. (**A**) $(\alpha hv)^2$-E plot of the $Cs_xFA_{1-x}PbI_{1.8}Br_{1.2}$ perovskite films. (**B**) Relationship between Cs molar fraction x and tauc-plot bandgaps of $Cs_xFA_{1-x}PbI_{1.8}Br_{1.2}$ perovskite films.

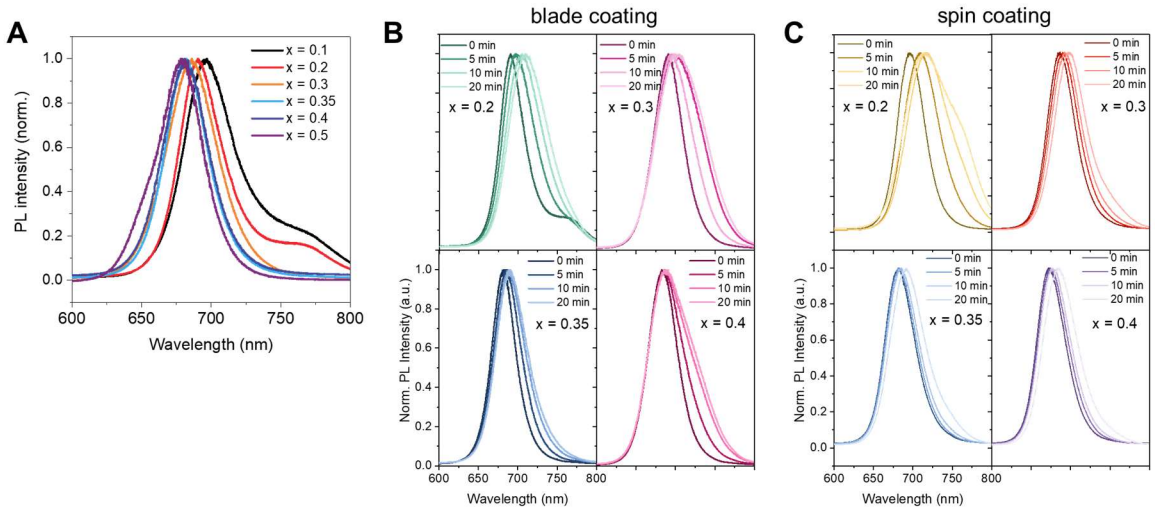

Fig. S11. (**A**) Photoluminescence (PL) spectra of blade-coated $Cs_xFA_{1-x}PbI_{1.8}Br_{1.2}$ perovskites; Photostability of $Cs_xFA_{1-x}PbI_{1.8}Br_{1.2}$ (x = 0.2~0.4) perovskites fabricated by (**B**) blade coating and (**C**) spin coating. PL spectral evolution of perovskite films was tracked under a high illumination intensity (532 nm laser, 1000 mW cm^{-2}) for various duration.

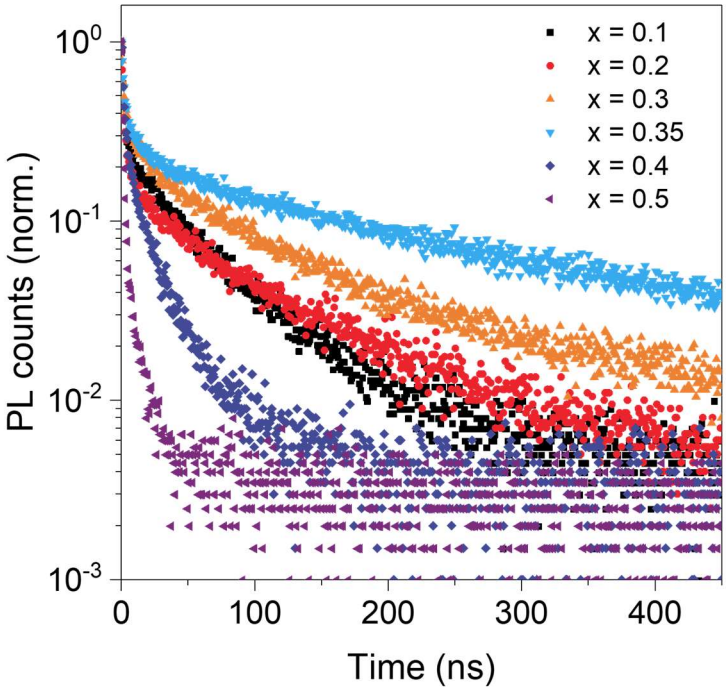

Fig. S12. Time-resolved PL spectra of $Cs_xFA_{1-x}PbI_{1.8}Br_{1.2}$ perovskite films.

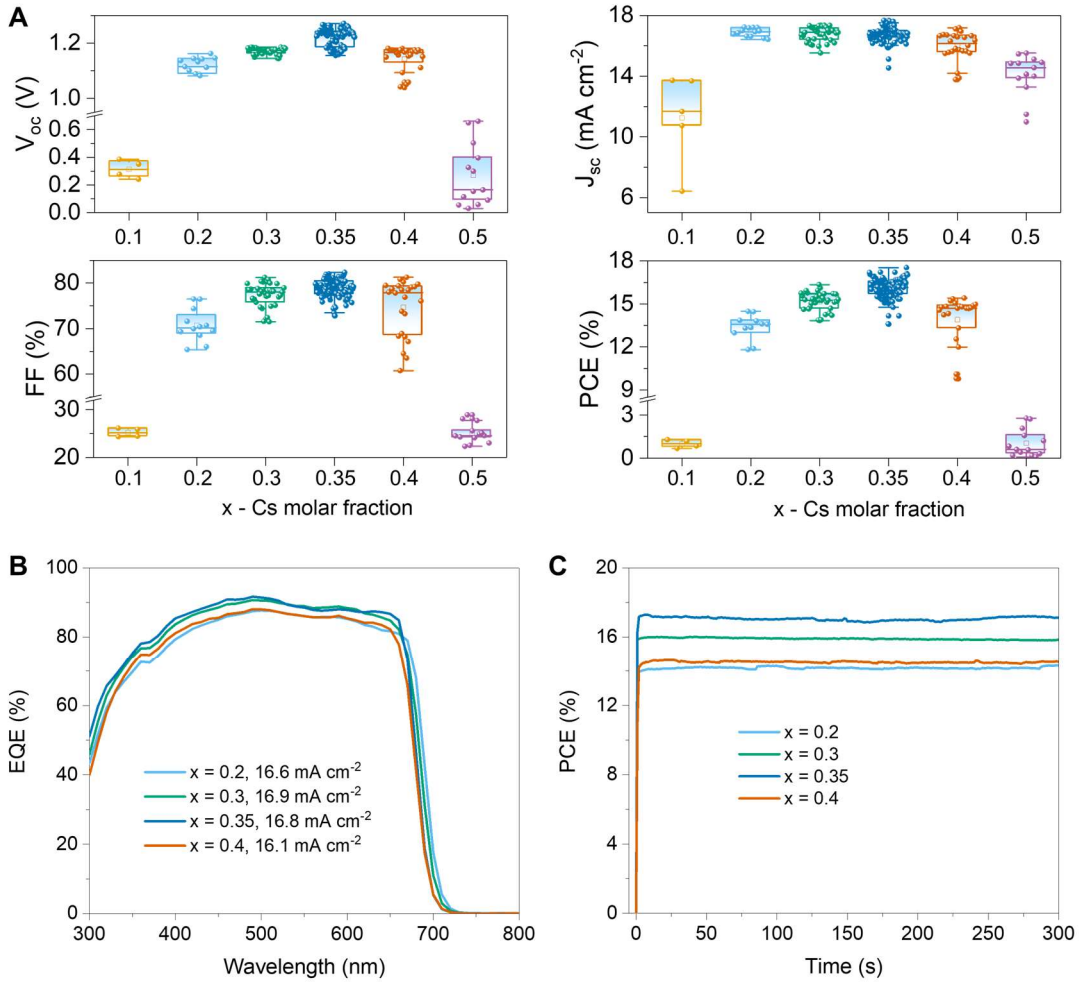

Fig. S13. Photovoltaic performance of $Cs_xFA_{1-x}PbI_{1.8}Br_{1.2}$ PSCs. (**A**) Performance statistics of $Cs_xFA_{1-x}PbI_{1.8}Br_{1.2}$ PSCs with various Cs molar fraction. The best performance (with an aperture area of 0.049 cm^2) was achieved at the Cs content of 0.35. (**B**) EQE spectra of the $Cs_xFA_{1-x}PbI_{1.8}Br_{1.2}$ PSCs. (**C**) Stabilized power output of $Cs_xFA_{1-x}PbI_{1.8}Br_{1.2}$ PSCs at the maximum power point.

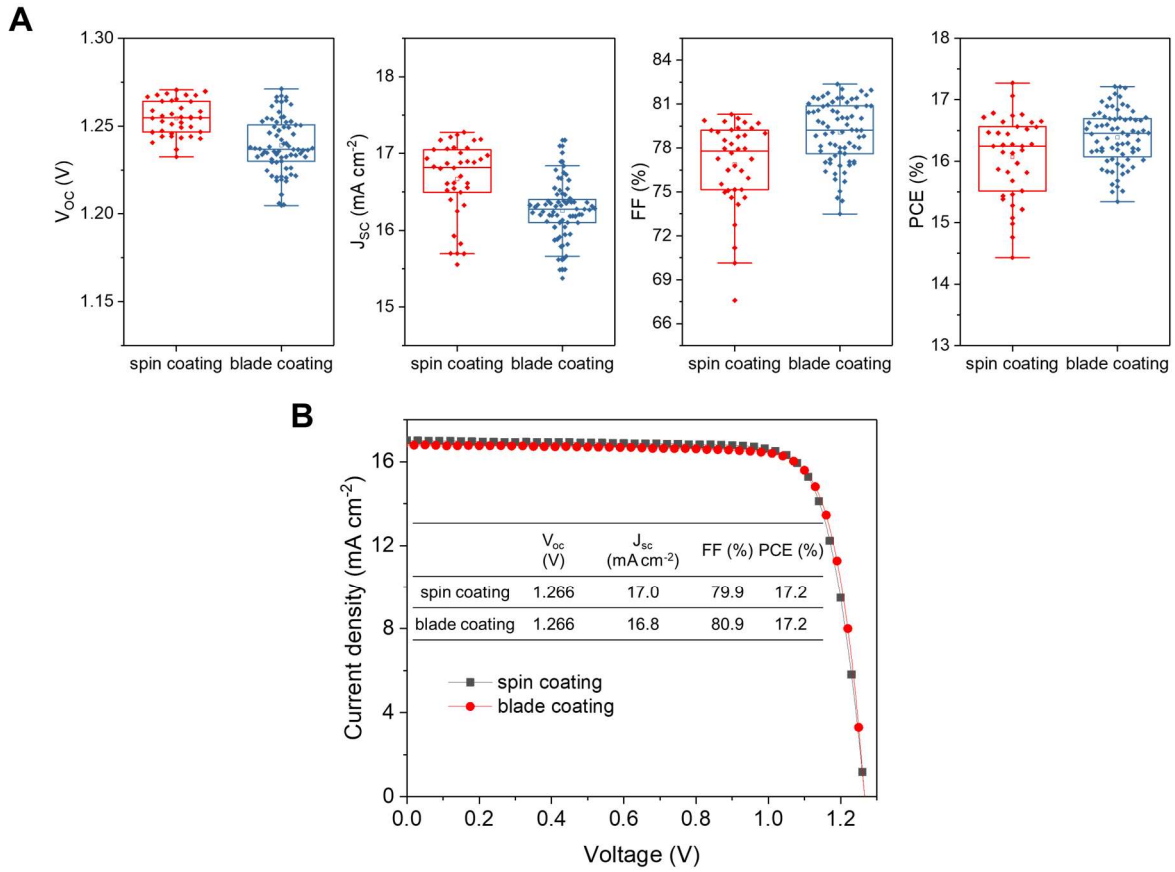

Fig. S14. Performance comparison of WBG PSCs by spin coating ($Cs_{0.2}FA_{0.8}PbI_{1.8}Br_{1.2}$) and blade coating ($Cs_{0.35}FA_{0.65}PbI_{1.8}Br_{1.2}$). (**A**) Comparison of photovoltaic performance between 38 spin-coated and 72 blade-coated WBG PSCs (aperture area 0.049 cm^2) processed over several identical runs. The box lines indicate the standard deviation and the center represents the mean value. (**B**) The J-V curves of the champion devices of spin-coated $Cs_{0.2}FA_{0.8}PbI_{1.8}Br_{1.2}$ and blade-coated $Cs_{0.35}FA_{0.65}PbI_{1.8}Br_{1.2}$ PSCs.

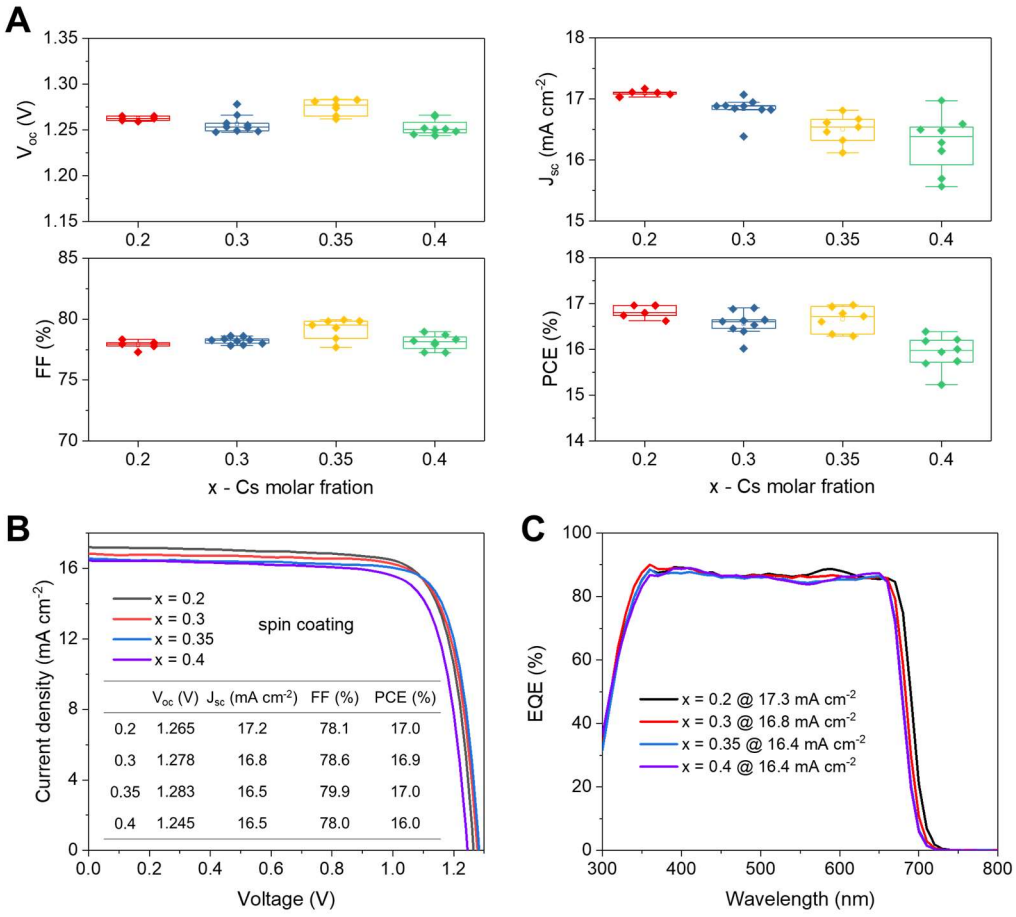

Fig. S15. Photovoltaic performance of spin-coated $Cs_xFA_{1-x}PbI_{1.8}Br_{1.2}$ PSCs. (**A**) Performance statistics of spin-coated $Cs_xFA_{1-x}PbI_{1.8}Br_{1.2}$ PSCs with various Cs contents. (**B**) J-V curves of the $Cs_xFA_{1-x}PbI_{1.8}Br_{1.2}$ PSCs. (**C**) EQE spectra of the $Cs_xFA_{1-x}PbI_{1.8}Br_{1.2}$ PSCs. The devices were measured with an aperture area of 0.049 cm^2.

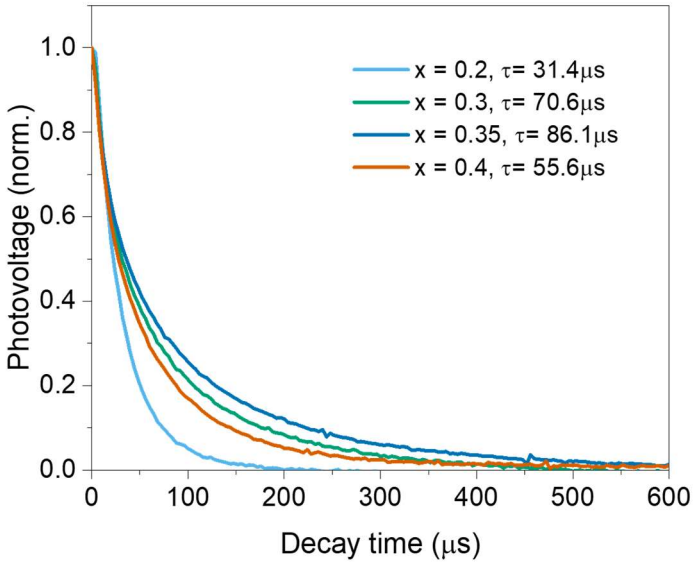

Fig. S16. Transient photovoltage decay of the $Cs_xFA_{1-x}PbI_{1.8}Br_{1.2}$ PSCs. The recombination lifetime (τ) is monoexponentially fitted.

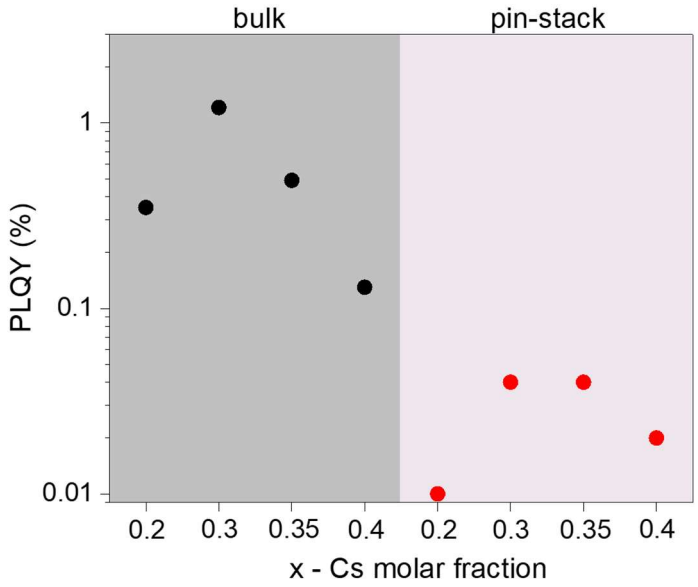

Fig. S17. Photoluminescence quantum yield (PLQY) analysis of the neat perovskite materials and corresponding pin-stacks.

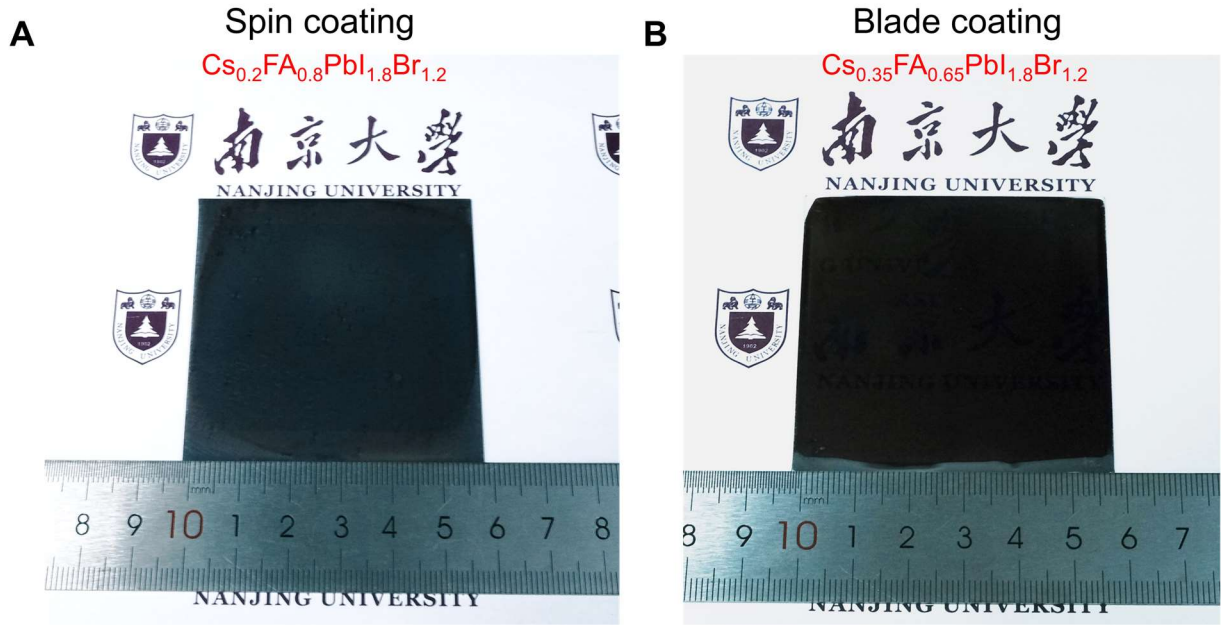

Fig. S18. Digital photos of the (**A**) spin-coated $Cs_{0.2}FA_{0.8}PbI_{1.8}Br_{1.2}$ and (**B**) blade-coated $Cs_{0.35}FA_{0.65}PbI_{1.8}Br_{1.2}$ perovskite films deposited on the 6 cm-by-6 cm substrates.

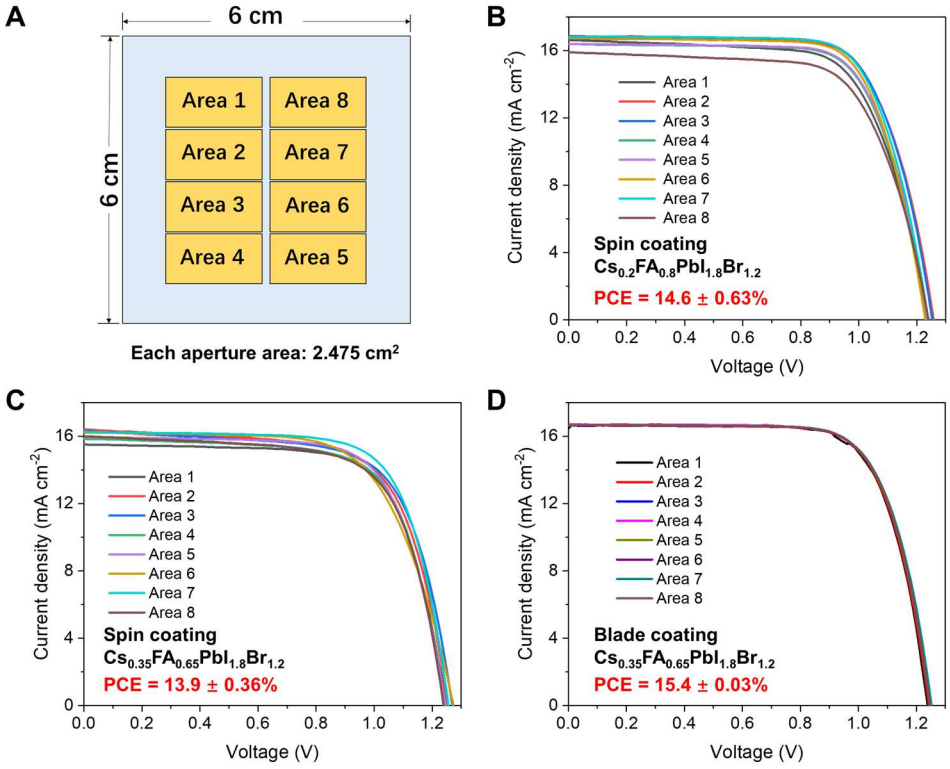

Fig. S19. (**A**) 8 individual PSCs (aperture area of 2.475 cm^2) deposited on 6 cm by 6 cm substrate. J-V curves of corresponding 8 PSCs using (**B**) spin-coated $Cs_{0.2}FA_{0.8}PbI_{1.8}Br_{1.2}$, (**C**) spin-coated $Cs_{0.35}FA_{0.65}PbI_{1.8}Br_{1.2}$ and (**D**) blade-coated $Cs_{0.35}FA_{0.65}PbI_{1.8}Br_{1.2}$.

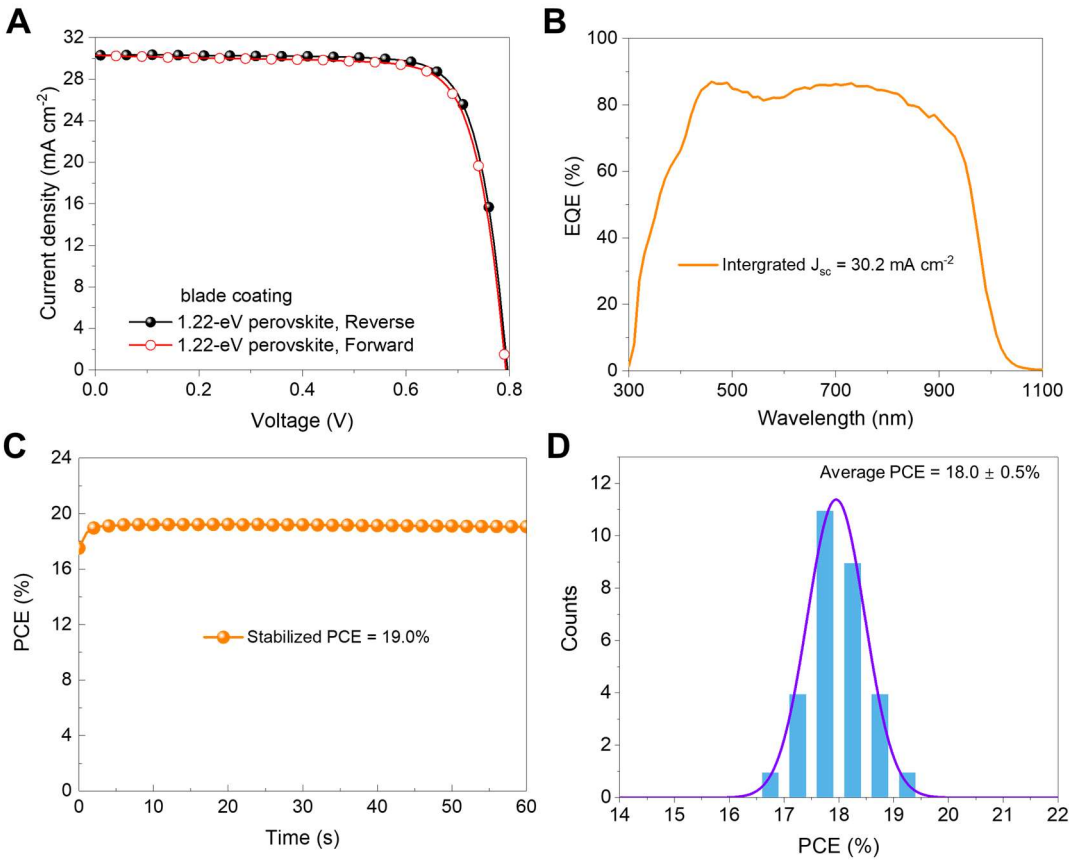

Fig. S20. Photovoltaic performance of the NBG ($MA_{0.3}FA_{0.7}Pb_{0.5}Sn_{0.5}I_3$) PSCs using blade-coated NBG perovskite films. (**A**) J-V curves of the champion NBG PSC. (**B**) EQE curve of the corresponding device. (**C**) Stabilized power output of the corresponding champion device. (**D**) reproductivity of the blade-coated NBG PSCs. It shows the PCE histogram of 30 devices, exhibiting an average PCE of 18.0 ± 0.5%.

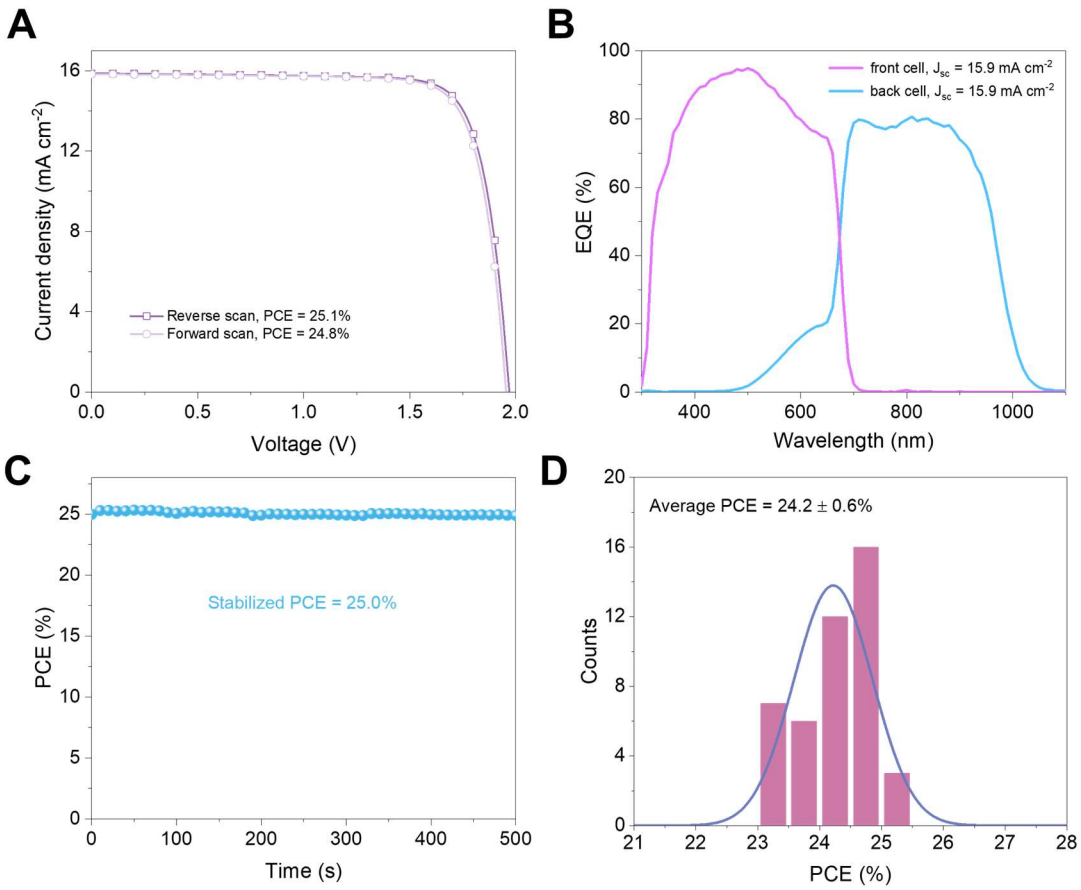

Fig. S21. Photovoltaic performance of the all-perovskite tandem solar cells using scalable procedures. (**A**) J-V curves of the champion tandem device. (**B**) EQE curve of the corresponding device. (**C**) Stabilized power output of the corresponding champion device. (**D**) reproductivity of the tandem devices. It shows the PCE histogram of 44 tandem devices, exhibiting an average PCE of 24.2 ± 0.6%.

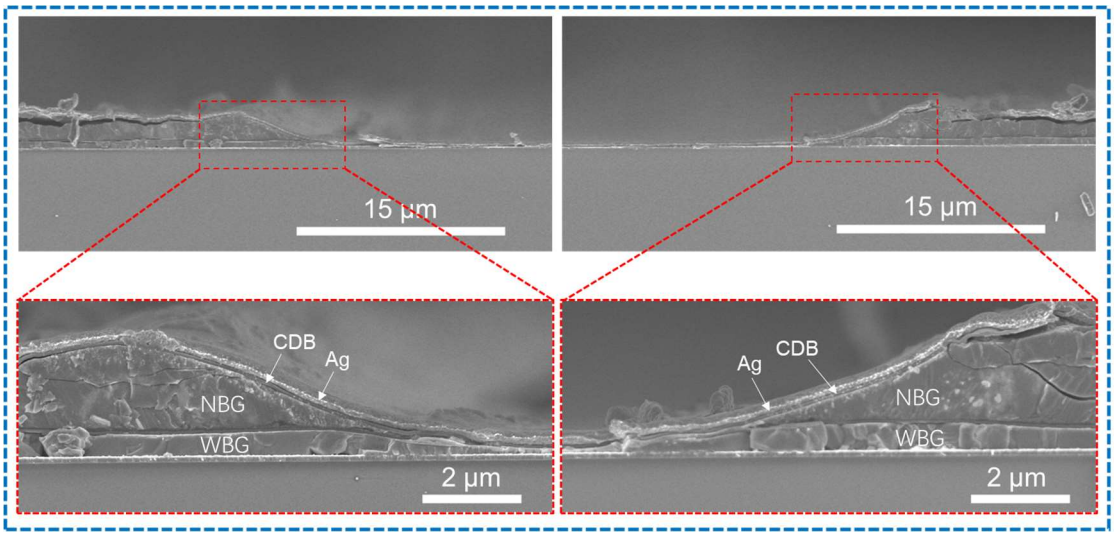

Fig. S22. Cross-sectional SEM images of the interconnection region in the module.

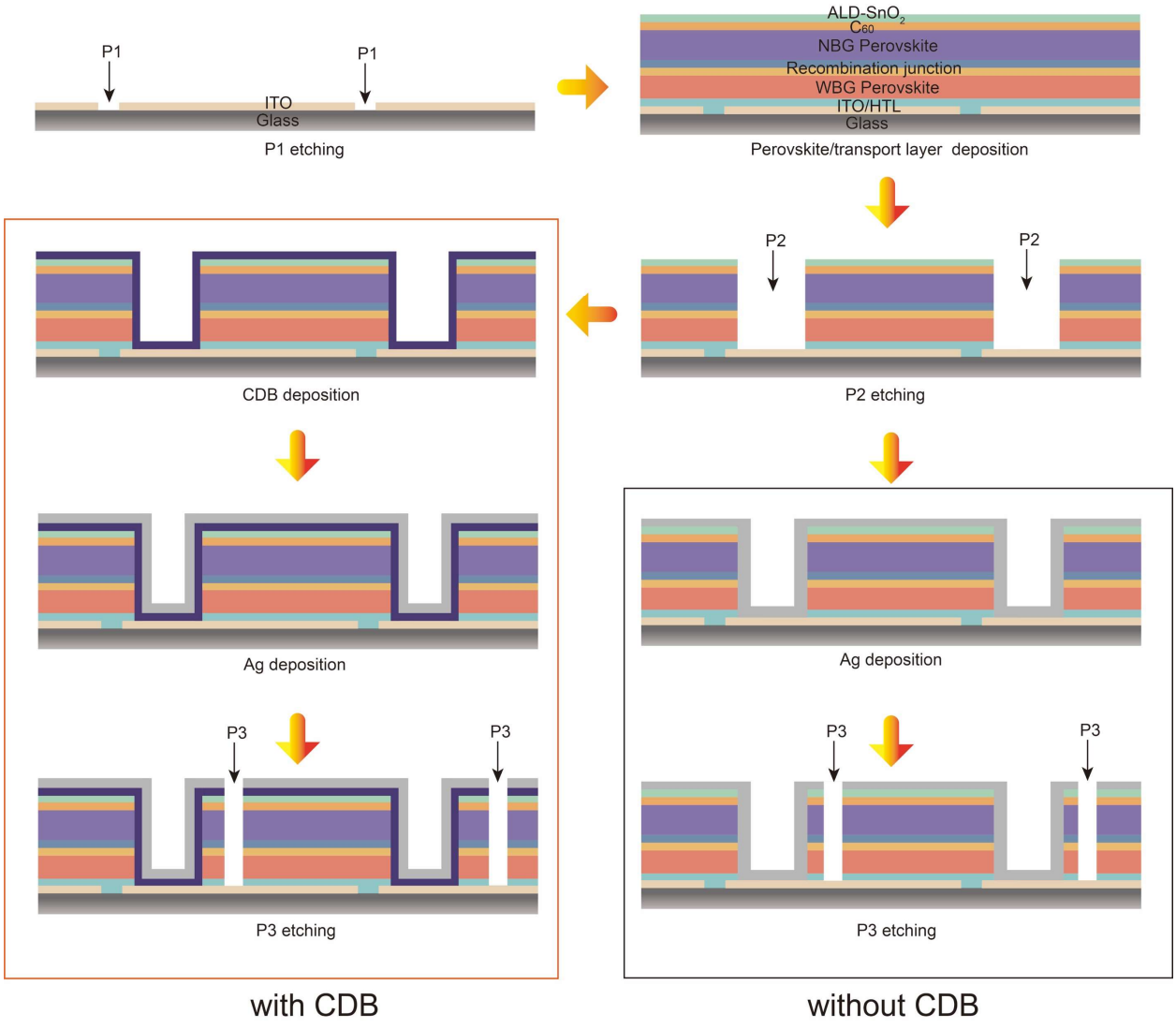

Fig. S23. Manufacturing process of the all-perovskite tandem solar modules with and without CDB. The thickness of SnO_2 layer on C_{60} (before P2) is ~15 nm. The thickness of CDB layer after P2 is ~10 nm.

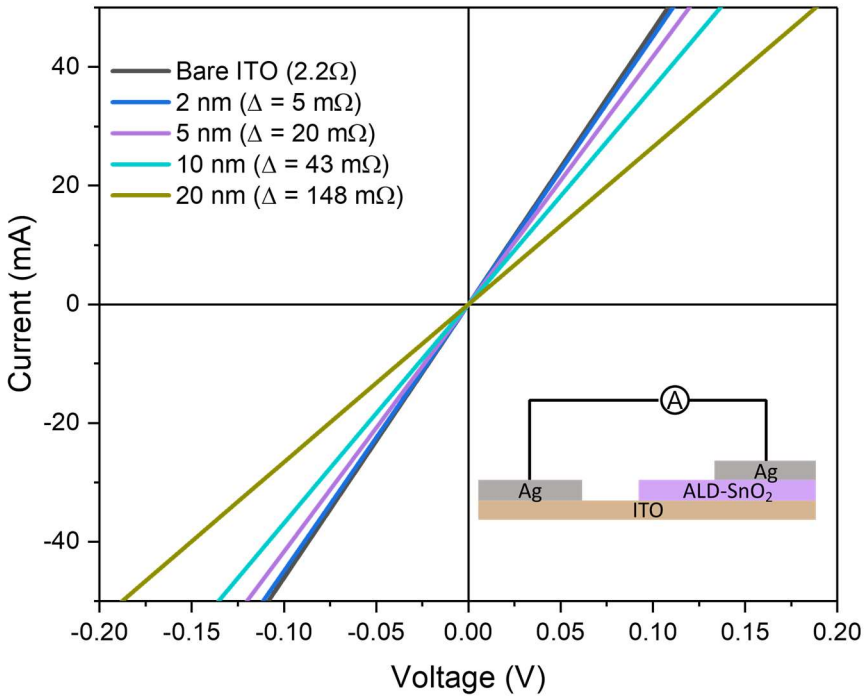

Fig. S24. Conductivity of the CDB layer. The I-V curve shows an ohmic contact in the device with the structure of ITO/ALD-SnO_2/Ag insert. The vertical resistance of CDB is negligible compared with bare ITO.

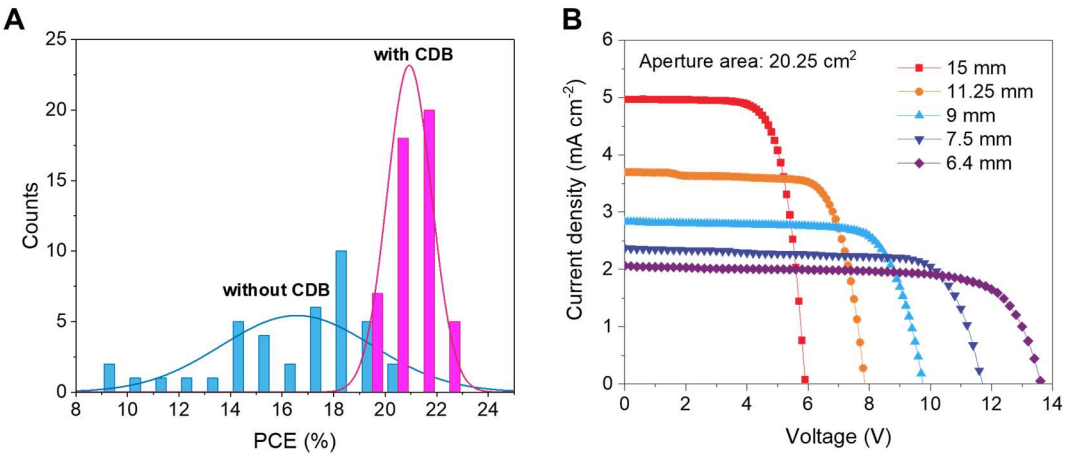

Fig. S25. Optimization for all-perovskite tandem modules. (**A**) PCE distribution of 40 modules without CDB and 50 modules with CDB. (**B**) J-V curves of the various modules (aperture area = 20.25 cm^2) with different width of subcells (corresponding to 3, 4, 5, 6 and 7 subcells).

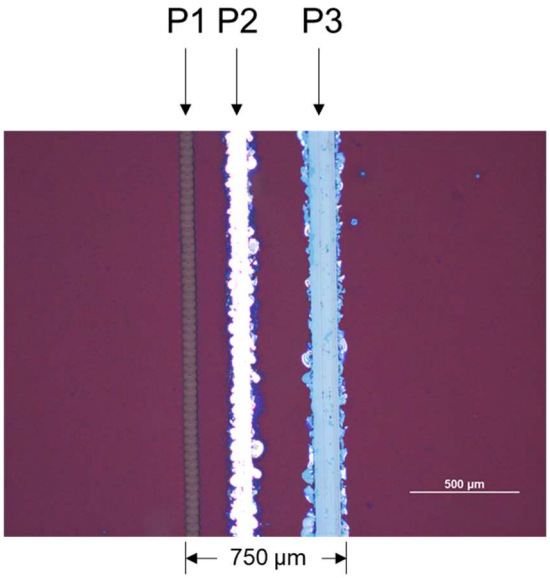

Fig. S26. Optical photo of scribing for subcell separation in modules. P1 patterning is processed by laser scribing with a width of ~50 µm, P2 and P3 etching are processed by mechanical scribing using a needle pen, which caused crude edge of P2 and P3.

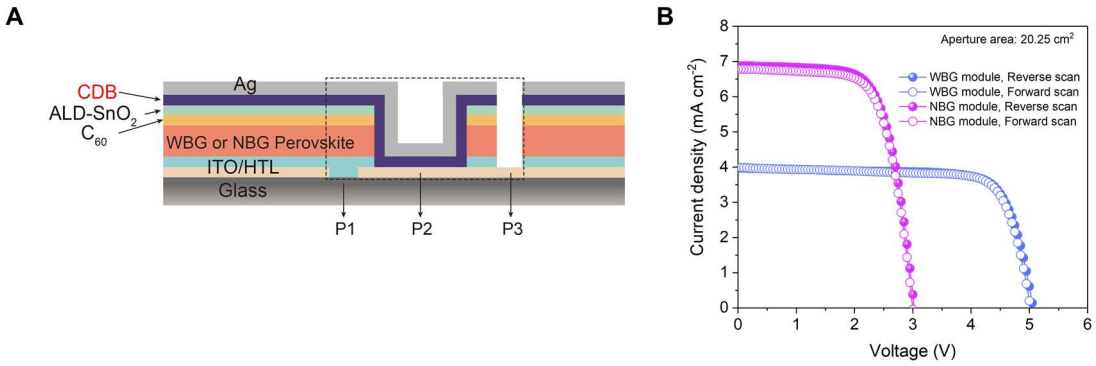

Fig. S27. WBG and NBG perovskite single-junction modules. (**A**) Structure schematic diagram of the series connected WBG or NBG perovskite module. (**B**) J-V curves of the WBG and NBG perovskite single-junction modules with an aperture area of 20.25 cm^2. The photovoltaic parameters are summarized in table S5.

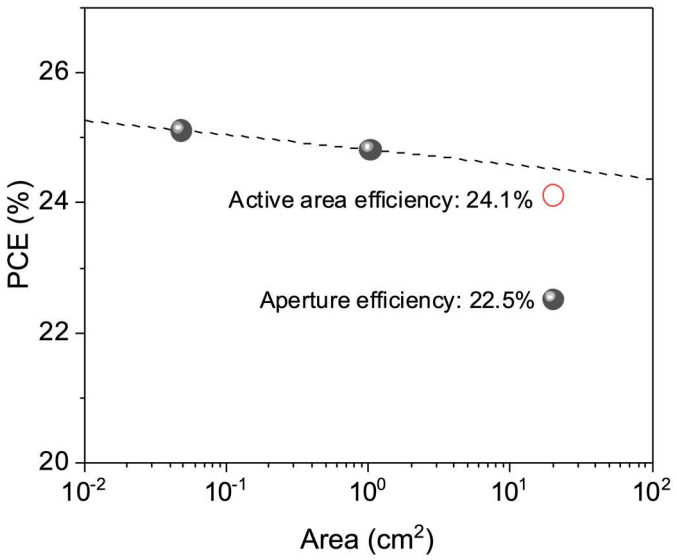

Fig. S28. Relationship between efficiency and device area. Considering a GFF of 93.3%, the active area efficiency of the champion 22.5%-efficient module is 24.1%. Dashed line is defined as the utmost efficiency with ideal uniformity.

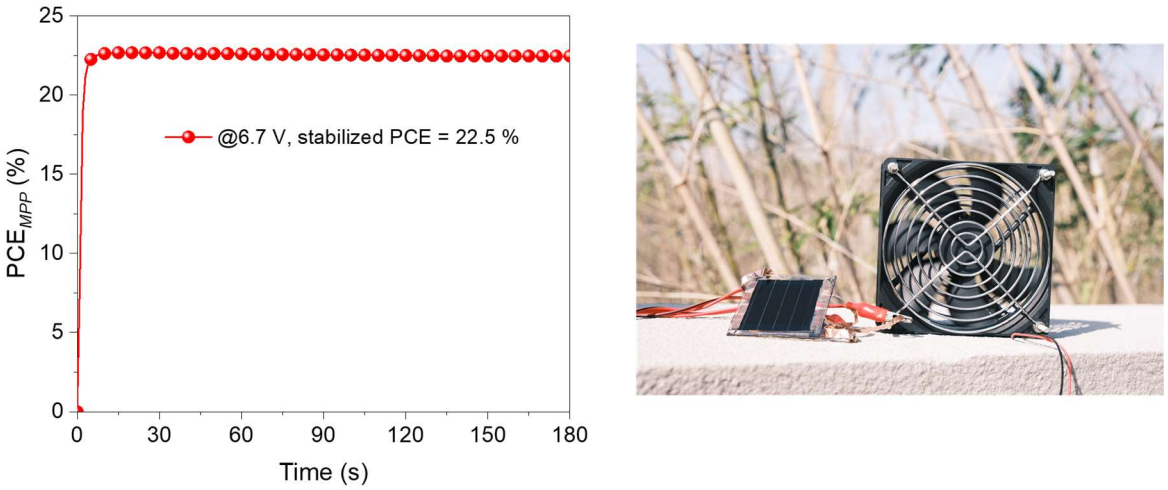

Fig. S29. Steady-state maximum power point (MPP) output of the champion module with CDB. The right photo shows that the module can drive a fan under the direct sunlight.

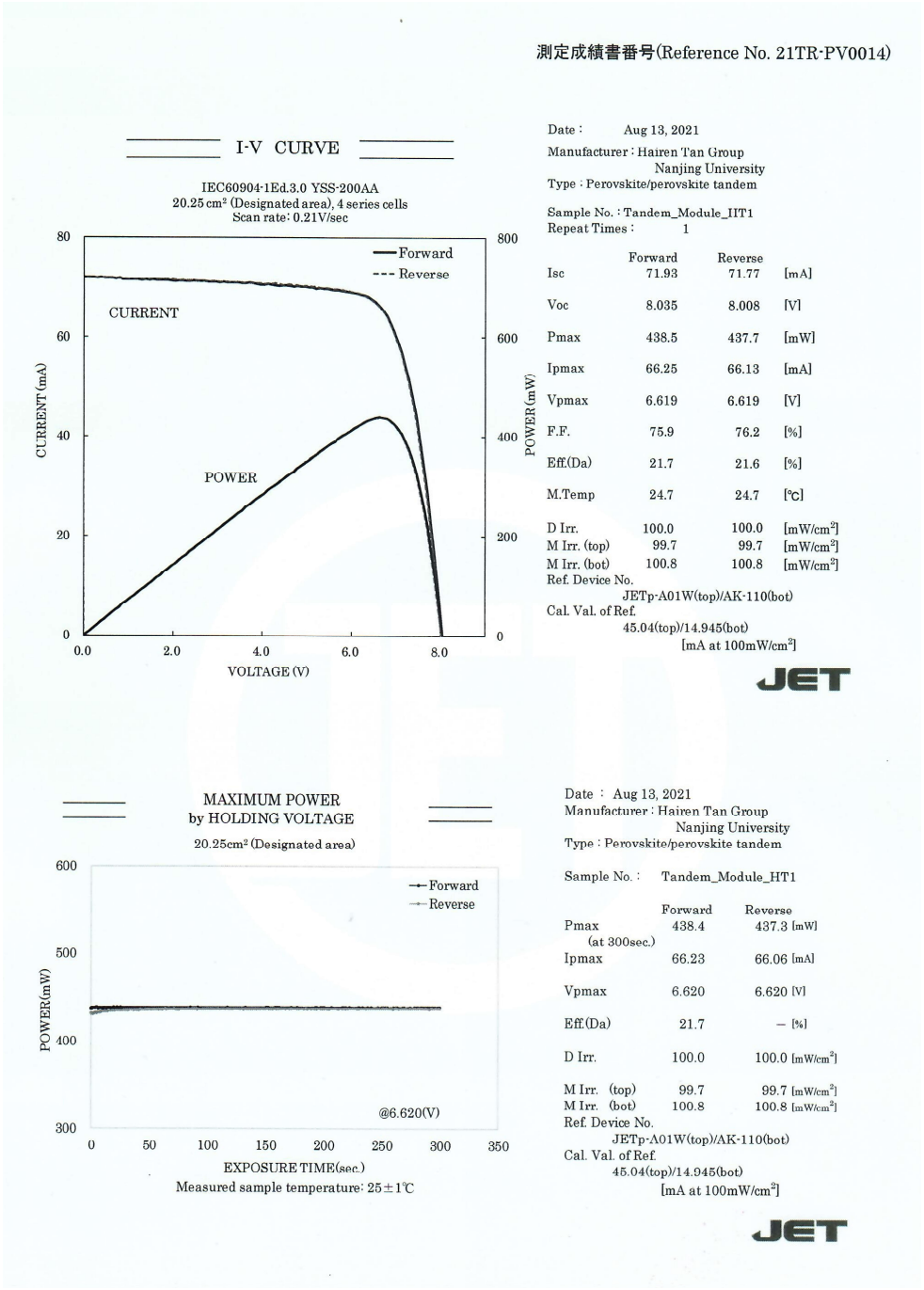

Fig. S30. The certificated result of a 20.25-cm^2-area all-perovskite tandem solar module measured by *JET*.

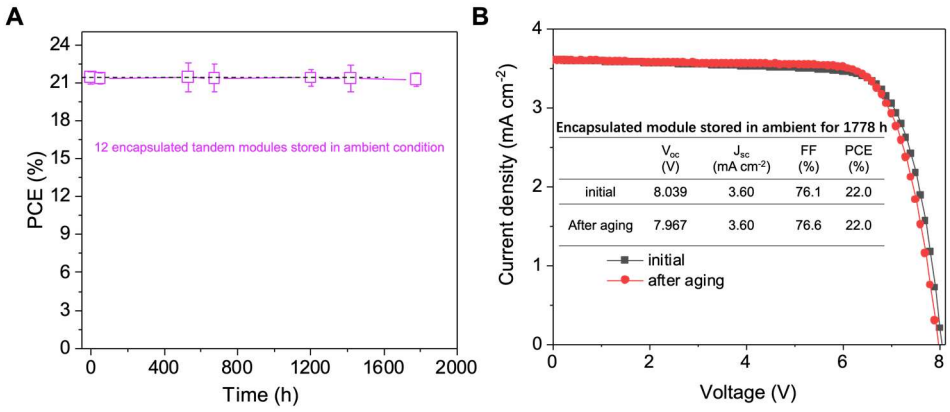

Fig. S31. Shelf stability of encapsulated all-perovskite tandem modules (aperture area of 20.25 cm^2) at ambient condition with humidity of ~40%. (**A**) Performance evolution of 12 tandem modules. The devices exhibited no obvious degradation in performance after storage for 1778 hours. (**B**) J-V curves of a 22.0%-efficiency tandem module before and after aging.

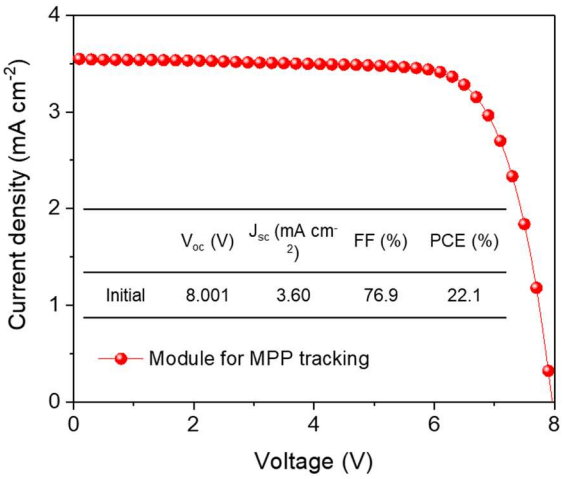

Fig. S32. Initial performance of the all-perovskite tandem module used for MPP tracking.

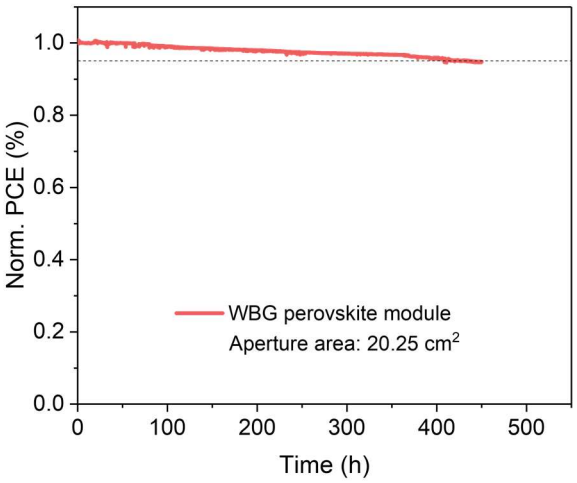

Fig. S33. Continuous MPP tracking of an encapsulated WBG perovskite single-junction module (aperture area: 20.25 cm^2) over 450 h under full simulated AM1.5G illumination (100 mW cm^{-2}, LED simulator) without an ultraviolet filter in ambient air with a humidity of 30-50%.

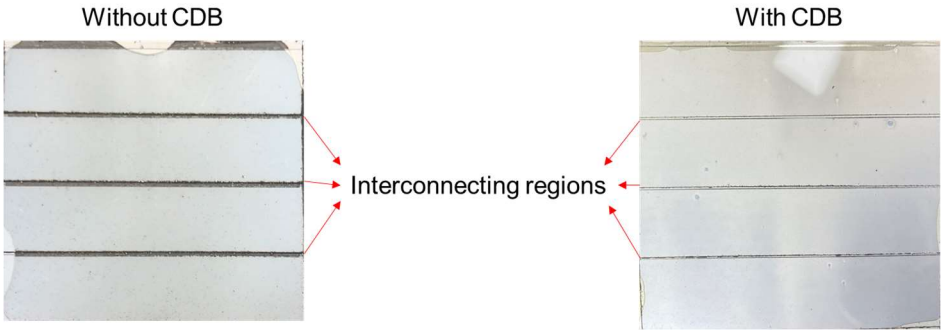

Fig. S34. Digital photos of the tandem modules with encapsulation after thermal aging in N_2 glove box.

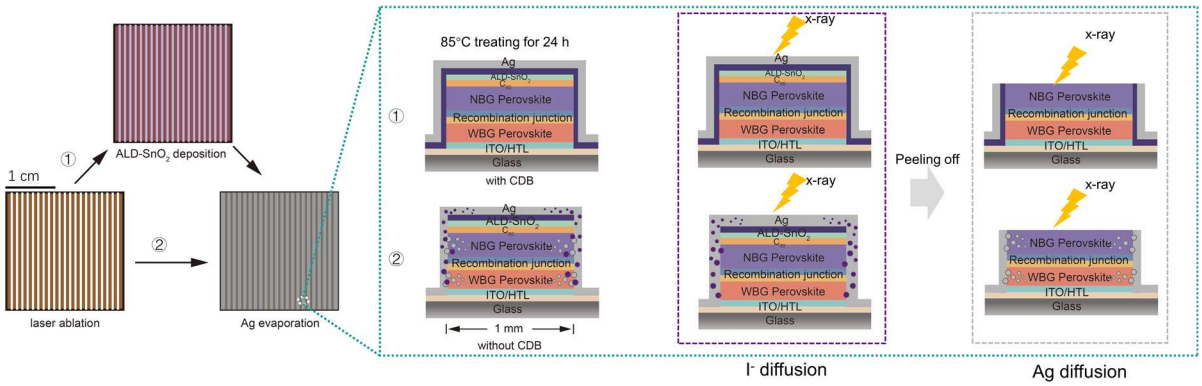

Fig. S35. Designed sample with reduced width of subcells at P2 process to obtain 1-mm width grid cell for I-Ag diffusion observation. For I^- diffusion characterization: The samples were preheated at 85°C for 24 h, then the samples were sent for XPS characterization. The x-ray beam is located at the center and top surface of the Ag-cover grid cell. For Ag diffusion characterization: The exposed perovskite surfaces with C_{60}/ALD-SnO_2/Ag peeled using tape and dichlorobenzene washing were sent for XPS characterization. The x-ray beam is located at the center and top surface of the exposed perovskites.

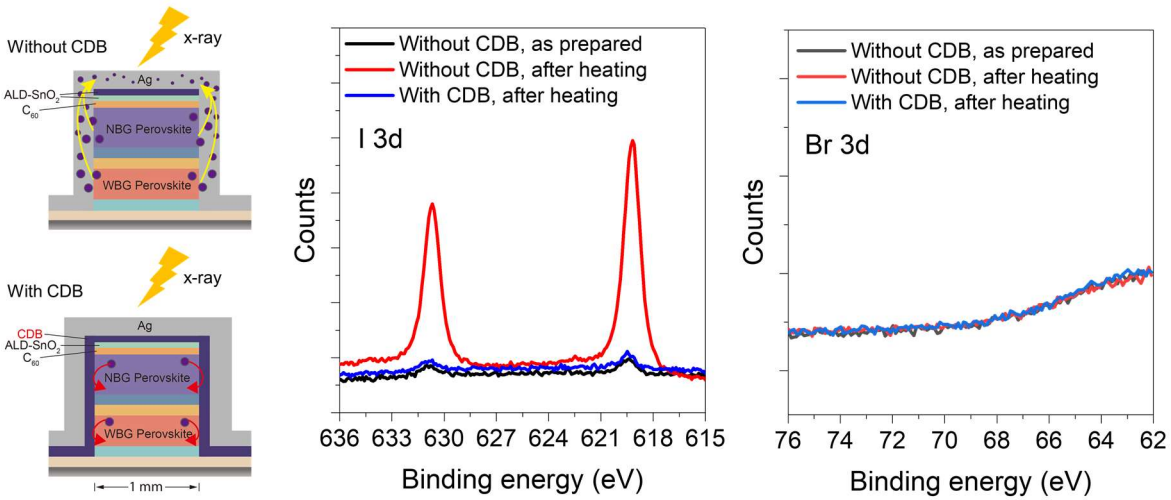

Fig. S36. The I 3d and Br 3d XPS spectra of the Ag-covered device surface. Illustrations on the left are the designed samples with reduced width of subcells at P2 process to obtain 1-mm width grid cell for halide-Ag interdiffusion observation (fig. S34).

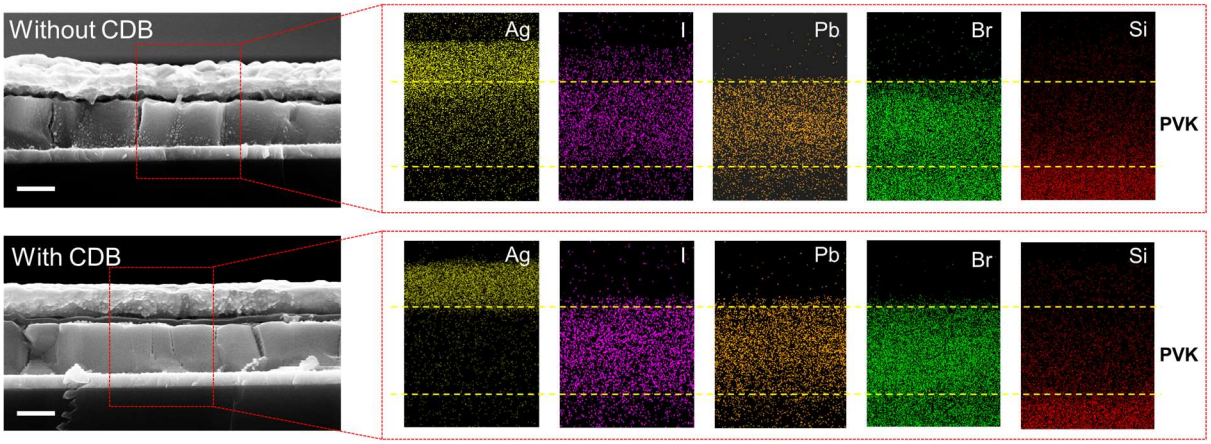

Fig. S37. SEM-EDX analysis of halide-Ag interdiffusion using the equivalent structure of glass/WBG perovskite/Ag with or without CDB insert at the interface between perovskite and Ag. The scale bar in SEM images is 300 nm. PVK: perovskite layer.

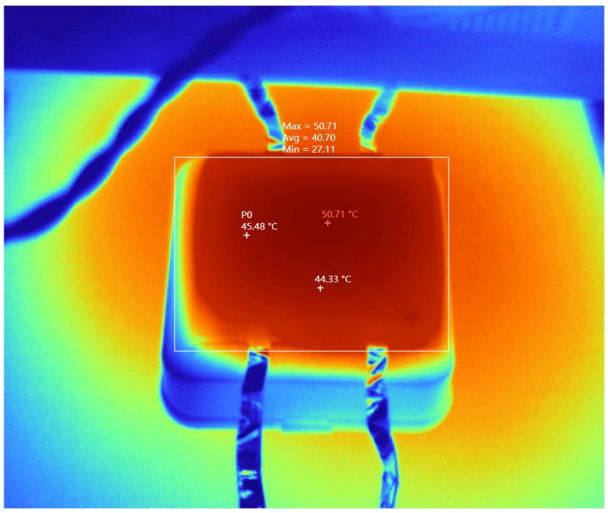

Fig. S38. Thermal image of the MPP-tracking tandem module. The working module shows an average temperature of 40.7°C with a peak temperature of 50.71°C and a valley temperature of 27.11°C. The image is taken by a Fluke thermal camera.

Table S1. Champion photovoltaic parameters of $Cs_xFA_{1-x}PbI_{1.8}Br_{1.2}$ perovskite solar cells as shown in Fig. 1D.

x	Bandgap (eV)	V_{oc} (V)	J_{sc} (mA cm^{-2})	FF (%)	PCE (%)
0.2	1.783	1.115	16.6	76.5	14.2
0.3	1.797	1.181	16.9	79.9	15.9
0.35	1.804	1.266	16.8	80.9	17.2
0.4	1.808	1.180	16.1	76.9	14.6

Table S2. Photovoltaic parameters of 8 individual PSCs measured from the spin-coated $Cs_{0.2}FA_{0.8}PbI_{1.8}Br_{1.2}$, spin-coated $Cs_{0.35}FA_{0.65}PbI_{1.8}Br_{1.2}$ and blade-coated $Cs_{0.35}FA_{0.65}PbI_{1.8}Br_{1.2}$ perovskite solar cells on 6 cm by 6 cm substrate as shown in fig. S19.

		V_{oc} (V)	J_{sc} (mA cm^{-2})	FF (%)	PCE (%)	PCE Standard deviation (%)
Spin coated $Cs_{0.2}FA_{0.8}PbI_{1.8}Br_{1.2}$	Area 1	1.238	16.63	68.50	14.10	0.63
	Area 2	1.258	16.85	71.42	15.14	
	Area 3	1.253	16.85	72.02	15.21	
	Area 4	1.236	16.38	71.57	14.48	
	Area 5	1.238	16.39	71.65	14.54	
	Area 6	1.230	16.71	72.68	14.93	
	Area 7	1.240	16.82	72.70	15.16	
	Area 8	1.240	15.89	68.06	13.42	
Spin coated $Cs_{0.35}FA_{0.65}PbI_{1.8}Br_{1.2}$	Area 1	1.248	15.50	70.49	13.64	0.36
	Area 2	1.254	16.41	68.23	14.04	
	Area 3	1.270	16.29	68.43	14.16	
	Area 4	1.239	15.85	70.04	13.75	
	Area 5	1.247	15.96	70.51	14.03	
	Area 6	1.273	16.21	66.16	13.65	
	Area 7	1.256	16.27	71.71	14.65	
	Area 8	1.239	15.98	68.62	13.59	
Blade coated $Cs_{0.35}FA_{0.65}PbI_{1.8}Br_{1.2}$	Area 1	1.239	16.65	74.19	15.31	0.03
	Area 2	1.243	16.92	72.98	15.35	
	Area 3	1.248	16.83	73.25	15.39	
	Area 4	1.248	16.88	72.98	15.38	
	Area 5	1.246	16.86	73.20	15.39	
	Area 6	1.248	16.83	73.28	15.39	
	Area 7	1.252	16.84	73.07	15.40	
	Area 8	1.247	16.84	73.28	15.38	

Table S3. Photovoltaic parameters of all-perovskite tandem modules (aperture area: 20.25 cm^2) with subcell number from 3 to 7 as shown in fig. S25B.

	Width of each subcell (mm)	V_{oc} (V)	J_{sc} (mA cm^{-2})	FF (%)	PCE (%)	Geometric FF (%)
3 subcells	15	5.91	4.97	72.3	21.2	95.0
4 subcells	11.25	7.86	3.70	74.4	21.6	93.3
5 subcells	9	9.75	2.83	74.8	20.6	91.7
6 subcells	7.5	11.71	2.35	74.6	20.5	90.0
7 subcells	6.4	13.63	2.06	72.3	20.3	88.3

Table S4. Summarized parameters of publicly reported, independently certified perovskite solar modules with areas over 10 cm^2.

Time	Institution	Area (cm^2)	Width of subcells (mm)	sub cells	V_{oc} (V)	J_{sc} (mA cm^{-2})	FF (%)	PCE (%)	GFF (%)	Test Centre	Ref.
All-perovskite tandem module (**This work**)	**NJU**	**20.3**	**11.3**	**4**	**8.04**	**3.55**	**75.9**	**21.7**	**93.3**	**JET**	
Single-junction perovskite module	UNIST	31.0	5.0	10	11.67	2.30	65.4	17.5	94.4	Newport	(*30*)
	UNCarolina	18.1	6.5	5	5.81	4.25	78.0	19.3	92.0	NREL	(*22*)
		50.0	6.5	14	16.07	1.53	78.0	19.1	N/A	NREL	(*22*)
	UNCarolina	29.5	6.5	8	8.72	2.83	75.4	18.6	92.0	NREL	(*20*)
		44.4	6.5	11	12.91	1.83	76.2	18.0	N/A	NREL	(*20*)
	WNLO, HUST	20.8	N/A	N/A	1.08	20.63	74.3	16.6	92.7	Newport	(*10*)
	OIST	22.3	6.7	7	7.50	2.72	71.0	13.9	91.0	AIST	(*25*)
	SJTU	35.8	N/A	10	10.80	1.84	71.5	14.2	N/A	Newport	(*26*)
	UNCarolina	63.7	N/A	16	18.94	1.15	75.5	16.4	N/A	NREL	(*21*)
	SJTU	36.1	N/A	10	8.36	2.02	71.5	12.1	N/A	AIST	(*23*)

Table S5. Photovoltaic parameters WBG and NBG perovskite single-junction modules (Aperture area: 20.25 cm^2) as shown in fig. S27.

	Scan direction	V_{oc} (V)	J_{sc} (mA cm^{-2})	FF (%)	PCE (%)
$Cs_{0.35}FA_{0.65}PbI_{1.8}Br_{1.2}$ module	Reverse	5.06	3.97	76.7	15.4
	Forward	5.02	3.99	76.3	15.3
$FA_{0.7}MA_{0.3}Pb_{0.5}Sn_{0.5}I_3$ module	Reverse	3.02	6.88	68.5	14.3
	Forward	3.00	6.78	68.7	14.0

Table S6. Summary of all-perovskite tandem solar cells and modules with areas > 1cm^2.

References	Area (cm^2)	PCE (%) (in-Lab/certified)	Method	single cell or module
Snaith et al. (*1*)	1	13.8/-	spin coating	single cell
Tan et al. (*3*)	1.05	22.3/22.1	spin coating	single cell
Huang et al. (*46*)	1.15	22.2/-	spin coating	single cell
Tan et al. (*2*)	1.05	24.7/24.2	spin coating	single cell
	12	21.4/-	spin coating	single cell
Huang et al. (*47*)	0.94	24.2/-	spin coating	single cell
Tan et al. (*4*)	1.05	25.3/-	spin coating	single cell
This work	1.05	24.8/-	blade coating	single cell
	20.25	22.5/21.7	blade coating	module

References

1. G. E. Eperon, T. Leijtens, K. A. Bush, R. Prasanna, T. Green, J. T.-W. Wang, D. P. McMeekin, G. Volonakis, R. L. Milot, R. May, A. Palmstrom, D. J. Slotcavage, R. A. Belisle, J. B. Patel, E. S. Parrott, R. J. Sutton, W. Ma, F. Moghadam, B. Conings, A. Babayigit, H.-G. Boyen, S. Bent, F. Giustino, L. M. Herz, M. B. Johnston, M. D. McGehee, H. J. Snaith, Perovskite-perovskite tandem photovoltaics with optimized band gaps. *Science* **354**, 861–865 (2016).

2. K. Xiao, R. Lin, Q. Han, Y. Hou, Z. Qin, H. T. Nguyen, J. Wen, M. Wei, V. Yeddu, M. I. Saidaminov, Y. Gao, X. Luo, Y. Wang, H. Gao, C. Zhang, J. Xu, J. Zhu, E. H. Sargent, H. Tan, All-perovskite tandem solar cells with 24.2% certified efficiency and area over 1 cm2 using surface-anchoring zwitterionic antioxidant. *Nat. Energy* **5**, 870–880 (2020).

3. R. Lin, K. Xiao, Z. Qin, Q. Han, C. Zhang, M. Wei, M. I. Saidaminov, Y. Gao, J. Xu, M. Xiao, A. Li, J. Zhu, E. H. Sargent, H. Tan, Monolithic all-perovskite tandem solar cells with 24.8% efficiency exploiting comproportionation to suppress Sn(ii) oxidation in precursor ink. *Nat. Energy* **4**, 864–873 (2019).

4. R. Lin, J. Xu, M. Wei, Y. Wang, Z. Qin, Z. Liu, J. Wu, K. Xiao, B. Chen, S. M. Park, G. Chen, H. R. Atapattu, K. R. Graham, J. Xu, J. Zhu, L. Li, C. Zhang, E. H. Sargent, H. Tan, All-perovskite tandem solar cells with improved grain surface passivation. *Nature* **603**, 73–78 (2022).

5. M. A. Green, E. D. Dunlop, J. Hohl-Ebinger, M. Yoshita, N. Kopidakis, X. Hao, Solar cell efficiency tables (version 59). *Prog. Photovoltaics Res. Appl.* **30**, 3–12 (2022).

6. J. E. Bishop, J. A. Smith, D. G. Lidzey, Development of Spray-Coated Perovskite Solar Cells. *ACS Appl. Mater. Interfaces* **12**, 48237–48245 (2020).

7. X. Peng, J. Yuan, S. Shen, M. Gao, A. S. R. Chesman, H. Yin, J. Cheng, Q. Zhang, D. Angmo, Perovskite and Organic Solar Cells Fabricated by Inkjet Printing: Progress and Prospects. *Adv. Funct. Mater.* **27**, 1703704 (2017).

8. Y. Deng, X. Zheng, Y. Bai, Q. Wang, J. Zhao, J. Huang, Surfactant-controlled ink drying enables high-speed deposition of perovskite films for efficient photovoltaic modules. *Nat. Energy* **3**, 560–566 (2018).

9. M. Yang, Z. Li, M. O. Reese, O. G. Reid, D. H. Kim, S. Siol, T. R. Klein, Y. Yan, J. J. Berry, M. F. A. M. van Hest, K. Zhu, Perovskite ink with wide processing window for scalable high-efficiency solar cells. *Nat. Energy* **2**, 17038 (2017).

10. Z. Yang, W. Zhang, S. Wu, H. Zhu, Z. Liu, Z. Liu, Z. Jiang, R. Chen, J. Zhou, Q. Lu, Z. Xiao, L. Shi, H. Chen, L. K. Ono, S. Zhang, Y. Zhang, Y. Qi, L. Han, W. Chen, Slot-die coating large-area formamidinium-cesium perovskite film for efficient and stable parallel solar module. *Sci. Adv.* **7**, eabg3749 (2021).

11. J. B. Whitaker, D. H. Kim, B. W. Larson, F. Zhang, J. J. Berry, M. F. A. M. Van Hest, K. Zhu, Scalable slot-die coating of high performance perovskite solar cells. *Sustain. Energy Fuels* **2**, 2442–2449 (2018).

12. J. Li, H. Wang, X. Y. Chin, H. A. Dewi, K. Vergeer, T. W. Goh, J. W. M. Lim, J. H. Lew, K. P. Loh, C. Soci, T. C. Sum, H. J. Bolink, N. Mathews, S. Mhaisalkar, A. Bruno, Highly Efficient Thermally Co-evaporated Perovskite Solar Cells and Mini-modules. *Joule* **4**, 1035–1053 (2020).

13. N.-G. Park, Crystal growth engineering for high efficiency perovskite solar cells. *CrystEngComm*. **18**, 5977–5985 (2016).

14. Y. Rong, Y. Hu, A. Mei, H. Tan, M. I. Saidaminov, S. Il Seok, M. D. McGehee, E. H. Sargent, H. Han, Challenges for commercializing perovskite solar cells. *Science* **361**, eaat8235 (2018).

15. Y. Hu, Y. Chu, Q. Wang, Z. Zhang, Y. Ming, A. Mei, Y. Rong, H. Han, Standardizing Perovskite Solar Modules beyond Cells. *Joule* **3**, 2076–2085 (2019).

16. E. Bi, H. Chen, F. Xie, Y. Wu, W. Chen, Y. Su, A. Islam, M. Grätzel, X. Yang, L. Han, Diffusion engineering of ions and charge carriers for stable efficient perovskite solar cells. *Nat. Commun.* **8**, 15330 (2017).

17. J. Li, Q. Dong, N. Li, L. Wang, Direct Evidence of Ion Diffusion for the Silver-Electrode-Induced Thermal Degradation of Inverted Perovskite Solar Cells. *Adv. Energy Mater.* **7**, 1602922 (2017).

18. H. Gao, Q. Lu, K. Xiao, Q. Han, R. Lin, Z. Liu, H. Li, L. Li, X. Luo, Y. Gao, Y. Wang, J. Wen, Z. Zou, Y. Zhou, H. Tan, Thermally Stable All-Perovskite Tandem Solar Cells Fully Using Metal Oxide Charge Transport Layers and Tunnel Junction. *Sol. RRL* **5**, 2100814 (2021).

19. C. C. Boyd, R. Cheacharoen, K. A. Bush, R. Prasanna, T. Leijtens, M. D. McGehee, Barrier Design to Prevent Metal-Induced Degradation and Improve Thermal Stability in Perovskite Solar Cells. *ACS Energy Lett.* **3**, 1772–1778 (2018).

20. Y. Deng, S. Xu, S. Chen, X. Xiao, J. Zhao, J. Huang, Defect compensation in formamidinium–caesium perovskites for highly efficient solar mini-modules with improved photostability. *Nat. Energy* **6**, 633–641 (2021).

21. Y. Deng, C. H. Van Brackle, X. Dai, J. Zhao, B. Chen, J. Huang, Tailoring solvent coordination for high-speed, room-temperature blading of perovskite photovoltaic films. *Sci. Adv.* **5**, eaax7537 (2019).

22. S. Chen, X. Dai, S. Xu, H. Jiao, L. Zhao, J. Huang, Stabilizing perovskite-substrate interfaces for high-performance perovskite modules. *Science* **373**, 902–907 (2021).

23. H. Chen, F. Ye, W. Tang, J. He, M. Yin, Y. Wang, F. Xie, E. Bi, X. Yang, M. Grätzel, L. Han, A solvent-and vacuum-free route to large-area perovskite films for efficient solar modules. *Nature* **550**, 92–95 (2017).

24. N. G. Park, K. Zhu, Scalable fabrication and coating methods for perovskite solar cells and solar modules. *Nat. Rev. Mater.* **5**, 333–350 (2020).

25. Z. Liu, L. Qiu, L. K. Ono, S. He, Z. Hu, M. Jiang, G. Tong, Z. Wu, Y. Jiang, D. Y. Son, Y. Dang, S. Kazaoui, Y. Qi, A holistic approach to interface stabilization for efficient

perovskite solar modules with over 2,000-hour operational stability. *Nat. Energy* **5**, 596–604 (2020).

26. E. Bi, W. Tang, H. Chen, Y. Wang, J. Barbaud, T. Wu, W. Kong, P. Tu, H. Zhu, X. Zeng, J. He, S. Kan, X. Yang, M. Grätzel, L. Han, Efficient Perovskite Solar Cell Modules with High Stability Enabled by Iodide Diffusion Barriers. *Joule* **3**, 2748–2760 (2019).

27. A. F. Palmstrom, G. E. Eperon, T. Leijtens, R. Prasanna, S. N. Habisreutinger, W. Nemeth, E. A. Gaulding, S. P. Dunfield, M. Reese, S. Nanayakkara, T. Moot, J. Werner, J. Liu, B. To, S. T. Christensen, M. D. McGehee, M. F. A. M. van Hest, J. M. Luther, J. J. Berry, D. T. Moore, Enabling Flexible All-Perovskite Tandem Solar Cells. *Joule* **3**, 2193–2204 (2019).

28. D. Zhao, C. Chen, C. Wang, M. M. Junda, Z. Song, C. R. Grice, Y. Yu, C. Li, B. Subedi, N. J. Podraza, X. Zhao, G. Fang, R.-G. Xiong, K. Zhu, Y. Yan, Efficient two-terminal all-perovskite tandem solar cells enabled by high-quality low-bandgap absorber layers. *Nat. Energy* **3**, 1093–1100 (2018).

29. Z. Yang, Z. Yu, H. Wei, X. Xiao, Z. Ni, B. Chen, Y. Deng, S. N. Habisreutinger, X. Chen, K. Wang, J. Zhao, P. N. Rudd, J. J. Berry, M. C. Beard, J. Huang, Enhancing electron diffusion length in narrow-bandgap perovskites for efficient monolithic perovskite tandem solar cells. *Nat. Commun.* **10**, 4498 (2019).

30. J. W. Yoo, J. Jang, U. Kim, Y. Lee, S.-G. Ji, E. Noh, S. Hong, M. Choi, S. Il Seok, Efficient perovskite solar mini-modules fabricated via bar-coating using 2-methoxyethanol-based formamidinium lead tri-iodide precursor solution. *Joule* **5**, 2420–2436 (2021).

31. S. Jariwala, H. Sun, G. W. P. Adhyaksa, A. Lof, L. A. Muscarella, B. Ehrler, E. C. Garnett, D. S. Ginger, Local Crystal Misorientation Influences Non-radiative Recombination in Halide Perovskites. *Joule* **3**, 3048–3060 (2019).

32. Y. Zhao, P. Miao, J. Elia, H. Hu, X. Wang, T. Heumueller, Y. Hou, G. J. Matt, A. Osvet, Y.-T. Chen, M. Tarragó, D. de Ligny, T. Przybilla, P. Denninger, J. Will, J. Zhang, X. Tang, N. Li, C. He, A. Pan, A. J. Meixner, E. Spiecker, D. Zhang, C. J. Brabec, Strain-activated light-induced halide segregation in mixed-halide perovskite solids. *Nat. Commun.* **11**, 6328 (2020).

33. R. E. Beal, N. Z. Hagström, J. Barrier, A. Gold-Parker, R. Prasanna, K. A. Bush, D. Passarello, L. T. Schelhas, K. Brüning, C. J. Tassone, H. G. Steinrück, M. D. McGehee, M. F. Toney, A. F. Nogueira, Structural Origins of Light-Induced Phase Segregation in Organic-Inorganic Halide Perovskite Photovoltaic Materials. *Matter*. **2**, 207–219 (2020).

34. K. A. Bush, K. Frohna, R. Prasanna, R. E. Beal, T. Leijtens, S. A. Swifter, M. D. McGehee, Compositional Engineering for Efficient Wide Band Gap Perovskites with Improved Stability to Photoinduced Phase Segregation. *ACS Energy Lett.* **3**, 428–435 (2018).

35. L. A. Castriotta, M. Zendehdel, N. Yaghoobi Nia, E. Leonardi, M. Löffler, B. Paci, A. Generosi, B. Rellinghaus, A. Di Carlo, Reducing Losses in Perovskite Large Area Solar

Technology: Laser Design Optimization for Highly Efficient Modules and Minipanels. *Adv. Energy Mater.* **2103420**, 2103420 (2022).

36. S. H. Reddy, F. Di Giacomo, A. Di Carlo, Low-Temperature-Processed Stable Perovskite Solar Cells and Modules: A Comprehensive Review. *Adv. Energy Mater.* **2103534**, 2103534 (2022).

37. R. Prasanna, T. Leijtens, S. P. Dunfield, J. A. Raiford, E. J. Wolf, S. A. Swifter, J. Werner, G. E. Eperon, C. de Paula, A. F. Palmstrom, C. C. Boyd, M. F. A. M. van Hest, S. F. Bent, G. Teeter, J. J. Berry, M. D. McGehee, Design of low bandgap tin–lead halide perovskite solar cells to achieve thermal, atmospheric and operational stability. *Nat. Energy* **4**, 939–947 (2019).

38. J. Yang, X. Liu, Y. Zhang, X. Zheng, X. He, H. Wang, F. Yue, S. Braun, J. Chen, J. Xu, Y. Li, Y. Jin, J. Tang, C. Duan, M. Fahlman, Q. Bao, Comprehensive understanding of heat-induced degradation of triple-cation mixed halide perovskite for a robust solar cell. *Nano Energy* **54**, 218–226 (2018).

39. L. Vesce, M. Stefanelli, J. P. Herterich, L. A. Castriotta, M. Kohlstädt, U. Würfel, A. Di Carlo, Ambient Air Blade-Coating Fabrication of Stable Triple-Cation Perovskite Solar Modules by Green Solvent Quenching. *Sol. RRL* **5**, 2100073 (2021).

40. R. Swartwout, R. Patidar, E. Belliveau, B. Dou, D. Beynon, P. Greenwood, N. Moody, D. DeQuilettes, M. Bawendi, T. Watson, V. Bulovic, Predicting Low Toxicity and Scalable Solvent Systems for High-Speed Roll-to-Roll Perovskite Manufacturing. *Sol. RRL* **6**, 2100567 (2021).

41. Q. Han, Y. Wei, R. Lin, Z. Fang, K. Xiao, X. Luo, S. Gu, J. Zhu, L. Ding, H. Tan, Low-temperature processed inorganic hole transport layer for efficient and stable mixed Pb-Sn low-bandgap perovskite solar cells. *Sci. Bull.* **64**, 1399–1401 (2019).

42. J. C. de Mello, H. F. Wittmann, R. H. Friend, An improved experimental determination of external photoluminescence quantum efficiency. *Adv. Mater.* **9**, 230–232 (1997).

43. R. D. J. Oliver, Y.-H. Lin, A. J. Horn, C. Q. Xia, J. H. Warby, M. B. Johnston, A. J. Ramadan, H. J. Snaith, Thermally Stable Passivation toward High Efficiency Inverted Perovskite Solar Cells. *ACS Energy Lett.* **5**, 3336–3343 (2020).

44. J. S. W. Godding, A. J. Ramadan, Y.-H. Lin, K. Schutt, H. J. Snaith, B. Wenger, Oxidative Passivation of Metal Halide Perovskites. *Joule* **3**, 2716–2731 (2019).

45. T. Kirchartz, J. A. Márquez, M. Stolterfoht, T. Unold, Photoluminescence-Based Characterization of Halide Perovskites for Photovoltaics. *Adv. Energy Mater.* **10**, 1904134 (2020).

46. Z. Yu, Z. Yang, Z. Ni, Y. Shao, B. Chen, Y. Lin, H. Wei, Z. J. Yu, Z. Holman, J. Huang, Simplified interconnection structure based on C60/SnO2-x for all-perovskite tandem solar cells. *Nat. Energy* **5**, 657–665 (2020).

47. Z. Yu, X. Chen, S. P. Harvey, Z. Ni, B. Chen, S. Chen, C. Yao, X. Xun, S. Xu, G. Yang, Y. Yan, J. J. Berry, M. C. Beard, J. Huang, Gradient Doping in Sn-Pb Perovskites by Barium Ions for Efficient Single-junction and Tandem Solar Cells. *Adv. Mater.* 2110351

(2022). DOI: 10.1002/adma.202110351